Original Research Article

International journal of spray and combustion dynamics

International Journal of Spray and Combustion Dynamics
Volume 11: 1–23

DOI: 10.1177/1756827719856237
journals.sagepub.com/home/scd
SAGE

Excitation of the precessing vortex core by active flow control to suppress thermoacoustic instabilities in swirl flames

Finn Lückoff and Kilian Oberleithner

Abstract

In this study, we apply periodic flow excitation of the precessing vortex core at the centerbody of a swirl-stabilized combustor to investigate the impact of the precessing vortex core on flame shape, flame dynamics, and especially thermoacoustic instabilities. The current control scheme is based on results from linear stability theory that determine the precessing vortex core as a global hydrodynamic instability with its maximum receptivity to open-loop actuation located near the center of the combustor inlet. The control concept is first validated at isothermal conditions. This is of utmost importance for the proceeding studies that focus on the exclusive impact of the precessing vortex core on the combustion dynamics. Subsequently, the control is applied to reacting conditions considering lean premixed turbulent swirl flames. Considering thermoacoustically stable flames first, it is shown that the actuation locks onto the precessing vortex core when it is naturally present in the flame, which allows the precessing vortex core frequency to be controlled. Moreover, the control allows the precessing vortex core to be excited in conditions where it is naturally suppressed by the flame, which yields a very effective possibility to control the precessing vortex core amplitude. The control is then applied to thermoacoustically unstable conditions. Considering perfectly premixed flames first, it is shown that the precessing vortex core actuation has only a minor effect on the thermoacoustic oscillation amplitude. However, we observe a continuous increase of the thermoacoustic frequency with increasing precessing vortex core amplitude due to an upstream displacement of the mean flame and resulting reduction of the convective time delay. Considering partially premixed flames, the precessing vortex core actuation shows a dramatic reduction of the thermoacoustic oscillation amplitude. In consideration of the perfectly premixed cases, we suspect that this is caused by the precessing vortex core-enhanced mixing of equivalence ratio fluctuations at the flame root and due to a reduction of time delays due to mean flame displacement.

Keywords

Active flow control, precessing vortex core, thermoacoustic, swirl-stabilized combustion, flame dynamics

Date received: 20 December 2018; accepted: 10 May 2019

1. Introduction

In modern gas turbine combustors, flame stabilization is typically achieved by an aerodynamic feature of swirling flows known as vortex breakdown. This phenomenon gives rise to an inner recirculation zone (IRZ) and corresponding inner and outer shear layers. Especially, the inner shear layer is prone to a global hydrodynamic instability known as the precessing vortex core (PVC).[1] The PVC can be described as a single helical-shaped coherent structure (azimuthal wavenumber of unity) which meanders downstream along this shear layer.[2] The PVC is typically present in isothermal swirling jets. However, in reacting flows, it depends on the

Laboratory for Flow Instabilities and Dynamics, Institute of Fluid Dynamics and Technical Acoustics, Technische Universität Berlin, Berlin

Corresponding author:
Finn Lückoff, Laboratory for Flow Instabilities and Dynamics, Institute of Fluid Dynamics and Technical Acoustics, Technische Universität Berlin, Müller-Breslau-Str. 8, 10589 Berlin, Berlin.
Email: finn.lueckoff@tu-berlin.de

density stratification, and thus, the flame shape whether a PVC is present or not.[3–5]

Several studies show that the PVC considerably influences the dynamics of swirl flames.[6–8] In particular, the PVC affects vortex-flame interaction,[9] flame stabilization,[10] and flame shape transition in connection with flame lift-off.[11–14] It was shown that a PVC arises as soon as a V-shaped flame detaches from the burner outlet and transitions to a detached M-flame.[3–5,11,12] Moreover, it was further shown that the strong velocity fluctuations near the burner outlet induced by the PVC enhance the mixing of fuel and air.[15–17]

The interaction of the PVC with thermoacoustic instability is an open question and subject to several studies. Previous studies in isothermal swirling jets suggest that the PVC may modify the mean flow as such that axisymmetric shear-layer instabilities are damped,[18,19] which ultimately leads to a reduction of thermoacoustic instability.[20] Moreover, it was shown by Stöhr et al.[12] that a thermoacoustic instability may suppress the PVC in a premixed swirl-stabilized flame. Depending on the operating conditions, the strong interaction of thermoacoustic and PVC modes was observed to lead either to suppression or excitation of the helical coherent structure.[21–23] Besides this, the interaction between PVC and thermoacoustic oscillations can generate additional interaction components as well.[14,24] Moreover, it is highly plausible that the aforementioned mixing enhancement induced by the PVC has a strong effect on the attenuation of equivalence ratio fluctuations, which is a key driver for thermoacoustic instability. Furthermore, the mean flame shape plays an important role for thermoacoustic instability,[25] which can be modified by the PVC. These ideas will be further investigated in this work.

Within the analytic framework of linear stability analysis, the PVC is interpreted as the manifestation of a linear global hydrodynamic instability. Recent studies have shown that this linear framework not only predicts the PVC quantitatively correct, but allows and determines the flow regions of its origin at reacting and non-reacting conditions.[1,3–5,26–32] Moreover, the mean field stability analysis allows for the prediction of the receptivity of the global mode to open-loop actuation, which is of utmost importance for the current control approach.[28,29,33,34] This receptivity can be represented as a two-dimensional map revealing those regions of the flow where external periodic actuation has most influence on global modes.[28,32,34] This approach was applied to realistic swirling fuel injector flows that give rise to a PVC.[29,30] The authors showed that the receptivity of the helical PVC mode is highest upstream of the central recirculation zone on the jet centerline in the vicinity of the nozzle outlet and the centerbody.

These findings have motivated a new control concept that acts directly on the PVC. For this purpose, an actuator was designed that actuates a helical PVC mode in the region of highest receptivity. In a preliminary study of isothermal low-Reynolds-number flows, an actuation lance was used that allowed for excitation of mode $m = 1$ on the jet centerline upstream of the vortex breakdown bubble. Closed-loop control experiments confirmed the effectiveness of the control and reproduced the receptivity determined from linear stability theory.[35] In a next step, this control was modified so that it is applicable to highly turbulent flows of swirl-stabilized combustors at reacting conditions. For this purpose, the actuator was implemented in a centerbody upstream the flame and successfully tested at isothermal flow conditions.[36] Finally, the actuator and sensors were advanced to be heat resistant and successfully tested under reacting conditions.[37] With this newly developed technique, the idea is either to excite the PVC through open-loop control at conditions where is naturally suppressed or to damp the instability through closed-loop phasor control where it is naturally occurring. As the control applies at the most receptive region of the instability, this control works at minimal energy input.

A main disadvantage of the studies mentioned at the beginning is that the PVC, as a natural instability of the flow, cannot be controlled independently from all other flow and flame conditions. These studies, therefore, do not allow to conclude about the direct impact of the PVC on the different flame mechanisms. This leads to the motivation of this work, where flow control is applied to directly control the PVC without altering the remaining flow and flame dynamics. The control applied in this work is motivated by recent findings of linear stability theory.

The goal of the present work is to apply this control to influence and suppress thermoacoustic instabilities occurring in turbulent swirl flames. As the control exploits the natural instability of flow field, it is expected to be very effective. For this purpose, we consider thermoacoustically unstable flames where the PVC is naturally suppressed. Through open-loop actuation, we excite a PVC mode in a controlled manner and investigate its effect on thermoacoustic oscillations.

The flow and flame dynamics are measured using high-speed PIV and OH*-chemiluminescence and analyzed using temporal Fourier analysis and spectral POD.[38] Experiments are conducted at perfectly and partially premixed conditions to isolate the aforementioned effect of the PVC on mean field modifications and equivalence ratio fluctuations, respectively. The key questions that are addressed in this work are:

1. Can we excite a PVC at conditions where it is naturally suppressed?

2. Can we excite a PVC in the presence of thermoacoustic oscillations?
3. What is the influence of PVC excitation on thermoacoustic oscillations?

The paper is structured as follows: the experimental test rig is explained first, with a detailed description of the actuator unit and the applied measurement techniques. In the next section, we introduce the data analysis methodology including SPOD, Fourier analysis, and OH*-chemiluminescence-related deconvolution methods. The result section starts with the presentation of a lock-in study conducted at isothermal conditions that demonstrate the PVC actuation principal. Subsequently, we consider data from a detached M-shaped flame that naturally features a PVC and an attached V-shaped flame that features no PVC. Both flames are operated at thermoacoustically stable conditions first, and the PVC dynamics in the flame are discussed. This leads to the core of the current work dealing with the influence of the PVC actuation on the thermoacoustically unstable V-flame configuration operated at perfectly and partially premixed conditions. The identified mechanisms and control opportunities are summarized in the concluding section, and an outlook toward future investigations is given.

2. Experimental setup

In this section, the experimental setup with the integrated actuator is presented and explained. Moreover, the conducted pressure and time-resolved PIV and OH*-measurements are described including the experimental procedure and applied operating conditions.

2.1. Test rig

Figure 1 shows the test rig consisting of three sections, which are labeled in the figure with ①, ②, and ③. Section ① represents the actuation unit which is used to actuate a helical PVC mode with an azimuthal wavenumber of unity at the centerbody (Figure 2). The helical actuation is achieved by four circumferentially arranged 5 in loudspeakers (rated power of 100 W) that are driven with a phase shift of $\pi/2$ relative to one another. The loudspeakers, which are driven by a four channel power amplifier, are mounted to aluminum plenums with an orifice at the bottom to which the red tubes are connected. The air column in the red tubes is actuated by the loudspeakers at a single frequency with a constant amplitude as indicated by the red arrows. The oscillating air exits through four centerbody outlets that have a rectangular shape (9 mm wide and 1 mm high) and are placed 25 mm upstream of the mixing tube end. The parabolic shape of the centerbody provides unaffected

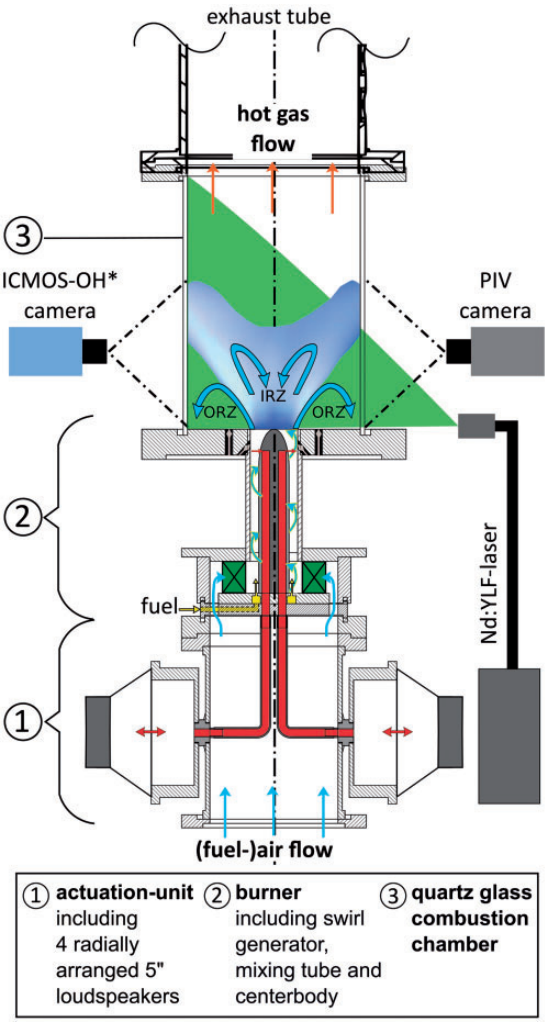

Figure 1. Test rig with measurement technique.

PVC dynamics, which is mandatory to obtain adequate experimental conditions.[36]

Section ② includes the burner, the swirl generator (green), the mixing tube with front plate, and the centerbody (in the center of the mixing tube). A detailed view of the burner setup is given in Figure 2. The yellow areas and arrows indicate the way of the fuel (natural gas) under partially premixed operating conditions. Under these operating conditions, the fuel is introduced downstream of the swirler directly into the mixing section. To achieve perfectly premixed operating conditions, the fuel is injected far upstream of the burner. The hydraulic diameter of the mixing tube $D_h = 20$ mm is equal to the difference between the outlet ($D = 55$ mm) and the centerbody diameter ($D_{CB} = 35$ mm). A radial swirl generator (marked green in Figures 1 and 2) is used to generate the swirling flow. This swirler consists of movable blocks which can be adjusted relative to each other.[39] In this way, the swirl number S, defined as the ratio of the axial flux of tangential momentum to the

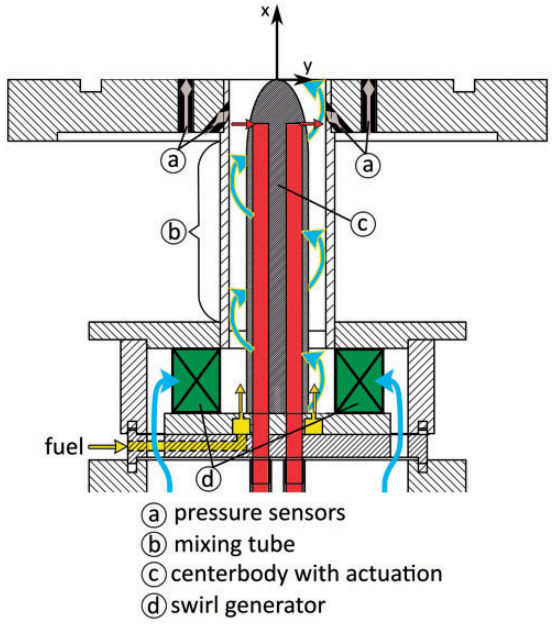

Figure 2. Detailed view of the burner.

axial flux of axial momentum, can be adjusted.[40] The swirl number was set to $S = 0.7$ in this study.

The combustion chamber (section ③ in Figure 1) consists of a cylindrical quartz glass tube with an inner diameter of 200 mm and a length of 300 mm. It provides optical access for the PIV and OH*-chemiluminescence measurements.

The origin of the coordinate system is set to the mixing tube outlet plane on the central jet axis (compare Figure 2). The x-coordinate points in axial direction, which is the main flow direction. Perpendicular to the axial coordinate, the y-coordinate describes the transverse or radial direction, respectively.

2.2. Experimental procedure

In this study, different operating conditions were investigated which are described by the equivalence ratio ϕ and the Reynolds number Re that is based on the hydraulic diameter of the mixing tube outlet and the bulk velocity at the outlet. For each operating condition, measurements were conducted with and without actuation. In case of a reacting flow, each measurement consists of time-resolved OH*-chemiluminescence and simultaneous pressure measurements.

The operating conditions are summarized in Table 1. Accordingly, a wide range of equivalence ratios were investigated. This results in different flame shapes, where only the detached flames at lean mixture naturally feature a PVC. The corresponding PVC frequencies are also listed in the table in real units and expressed as a Strouhal number based on the bulk velocity and the

Table 1. Operating conditions of reacting tests.

Reynolds number	Re	22000	26000	30000
Air mass flow [kg/h]		100	120	140
Natural PVC freq. [Hz]		118	138	163
Strouhal number	St	0.14		
Swirl number	S	0.7		
Equivalence ratio	ϕ	$0.59 \leq \phi \leq 0.74$		
Premix types	-	perfectly, partially		
Inlet temperature [K]		293		
Thermal power [kW]	P	$29 \leq P \leq 43$		

U_0 and hydraulic inlet diameter D_h. As also seen in the previous studies, the PVC frequency shows clear Strouhal number scaling with $St = 0.14$ for all cases considered.

The actuation frequencies selected in this study are close to the natural PVC frequencies to achieve optimal response by exploiting the natural instability. For the operating conditions, where the PVC is not naturally present (rich mixtures), actuation was applied at the same Strouhal numbers, assuming that the instability driving the PVC is not substantially changed. This assumption is supported by the comparison between reacting and non-reacting conditions, where the PVC frequency is quite robust showing only slight changes of less than 5%.

To quantify the actuator efficiency, it is common to relate the momentum of the actuation jets to the momentum of the main flow, yielding the momentum coefficient[41]

$$C_\mu = G u_{\mathrm{RMS}}^2 / \left(U_0^2 A_h\right) \tag{1}$$

where u_{RMS} represents the RMS velocity at the actuator outlet, which was measured with a hot-wire anemometer,[36] G the outlet area of the actuator, A_h the hydraulic cross section area, based on the hydraulic diameter of the mixing tube D_h, and U_0 the bulk velocity of the main flow. In the present work, the maximum actuation amplitude was set to $C_\mu = \{1.19, 0.83, 0.49\}\%$ for the three considered Reynolds numbers, respectively (see Table 1). These values were chosen based on preliminary open-loop experiments at isothermal conditions, and they were found to be sufficient to generate lock-in reliably without changing the mean flow considerably.

2.3. Measurement techniques

Time-resolved OH*-chemiluminescence measurements were conducted in the combustion chamber (Figure 1).

The recorded OH*-chemiluminescence images serve as a qualitative indicator for heat release rate and reveal the mean and phase-averaged flame shape. For these measurements, a high-speed CMOS camera (Photron SA 1.1) in combination with a high-speed intensifier (Lambert Instruments HiCATT 25) was used to capture line-of-sight OH*-chemiluminescence intensity snapshots. The camera was equipped with a 308 nm band pass filter to record only the OH*-chemiluminescence. The sampling rate of the camera was set to 1013 Hz to resolve the dynamics related to the PVC and occurring thermoacoustic oscillation, which are in the range of 70–180 Hz. Within a measurement time of approximately 2.1 s, 2183 snapshots with a resolution of 1024×1024 pixels were acquired.

In a separate experiment, time-resolved PIV measurements were conducted at isothermal conditions. Therefore, the same camera was used in connection with a high-speed Nd:YLF diode pumped laser (Quantronix Darwin Duo 527-100 M, 527 nm and total pulse energy of 60 mJ). A light sheet optic was used to generate an appropriated light sheet of approximately 1 mm thickness in the measurement area, which was seeded with solid TiO_2 particles. The recorded particle snapshots were evaluated with a commercial PIV software. The correlation scheme employs multigrid refinement[42] with a final window size of 16×16 pixels, window overlap of 50% in combination with spline-based image deformation,[43] and subpixel peak fitting. In the final step, the vector fields were filtered for outliers and interpolated from adjacent interrogation windows.

The pressure was measured by miniature differential pressure sensors (First Sensor HDOM010 with 1000 Pa range) which were arranged circumferentially at the outlet of the mixing tube (compare ⓐ in Figure 2). In each of the two pressure measurement planes, four sensors were mounted. In the mixing tube, the sensor orientation was shifted by 20° relative to the exit channels of the actuator to avoid interference with the actuation jets emanating from the centerbody. The pressure sensors were connected to the flow via short cannula tubes to allow for measuring pressure fluctuations as small as 0.1 Pa. All reference pressure ports of the differential sensors were connected to an ambient pressure reservoir to provide a common reference pressure. The signals were amplified with an in-house amplifier and digitized by a 16 bit A/D converter (NI 9216) at a sampling frequency of 16,384 Hz. In a previous study,[36] the accuracy of the PVC signal measured with the pressure sensors was estimated in comparison to the time coefficients of corresponding POD modes determined from time-resolved PIV measurements. The error was estimated at approximately 5% for the pressure sensor arrangement used in the present study.

3. Data analysis methodology

In the following, the reader is briefly introduced to spatial Fourier decomposition applied to the pressure signal as well as the post-processing of the PIV and OH*-chemiluminescence snapshots.

3.1. Spatial Fourier decomposition of the pressure signals

The pressure signals are used to characterize the amplitude and frequency of the PVC in the combustion chamber. The signals recorded by the four circumferentially arranged pressure sensors are decomposed into Fourier modes with azimuthal wavenumbers. Accordingly, the signal of the mth azimuthal mode is given as

$$\hat{p}_m(t) = \sum_{k=1}^{4} p_k(t) \exp\left(i2\pi m \frac{k}{4}\right) \tag{2}$$

where p_k is the pressure signal of the kth sensor and m the azimuthal wavenumber. With four circumferentially arranged sensors, azimuthal modes with wavenumbers $m = \{0, 1, 2\}$ can be detected. The Fourier coefficient $\hat{p}_m$ is complex and a function of time, where $m = 1$ describes the PVC dynamics, and the instantaneous amplitude and phase of the PVC correspond to the modulus and argument of $\hat{p}_1$, respectively.

3.2. Spectral proper orthogonal decomposition of time-resolved PIV snapshots

The spectral proper orthogonal decomposition (SPOD) is a recently introduced method to identify coherent structures in time-resolved flow data.[44] It is based on the classical proper orthogonal decomposition (POD),[45] but it offers a more precise selectivity of relevant modes, which provide benefits in complex turbulent flows like the combustor flow investigated here.[46] In the following, only a very brief description of the SPOD approach is given. A more detailed derivation can be found in Sieber et al.[44] The procedure is exemplified for the crosswise velocity V but holds similar for the axial velocity U. The SPOD provides a modal decomposition of the fluctuating part of the velocity V' that reads as follows

$$V(\mathbf{x}, t) = \bar{V}(\mathbf{x}) + V'(\mathbf{x}, t) = \bar{V}(\mathbf{x}) + \sum_{i=1}^{N} a_i(t)\Phi_i(\mathbf{x}) \tag{3}$$

The fluctuating part of the velocity is separated into a sum of spatial modes Φ_i and corresponding modal coefficients a_i. In order to build this basis, the spatial

correlation among individual PIV snapshots is calculated, which results in a corresponding correlation matrix. In contrast to the classical POD, a Gaussian low-pass filter is applied to this correlation matrix, which puts a temporal constraint on the POD modes. The width of this filter is typically related to the convection time of the most dominant structure, in this case, the PVC. The temporal coefficients $a_i(t)$, describing the dynamics of the corresponding mode, are derived from the eigenvectors of the filtered correlation matrix. The spatial modes $\Phi_i(\mathbf{x})$ are finally obtained from the projection of the snapshots onto the temporal coefficients.

3.3. Decomposition of the OH*-signal

The global heat release rate fluctuation is an important quantity to characterize the flame response to actuation and flow perturbations. The global heat release rate $I(t)$ is obtained by integrating the OH*-signal $\mathrm{OH}^*(x, y, t)$ recorded by the camera over the entire flame area. Time averaging of this quantity provides an estimate of the mean global heat release rate $\bar{I}$ and its temporal fluctuation $I'(t) = I(t) - \bar{I}$.

To differentiate between the global heat release rate fluctuations induced by thermoacoustic fluctuations and by the PVC, we employ a special decomposition method. By assuming that the mean flame is axisymmetric, the thermoacoustic modes induce heat release fluctuations $\mathrm{OH}^{*\prime}(x, y, t)$ which are symmetric with respect to the centerline of the combustor. Accordingly, the heat release fluctuations integrated over the left ($y < 0$) and right ($y > 0$) half of the combustion chamber are in phase. Contrarily, the PVC as a single-helical flow structure generates heat release fluctuations which are antisymmetric with respect to the centerline of the combustor. Consequently, the corresponding heat release fluctuations integrated over the left ($y < 0$) and right ($y > 0$) half of the combustion chamber are 180° out of phase. Hence, the summation of the heat release fluctuations left ($\mathrm{OH}^{*\prime}(x, y < 0, t)$) and right ($\mathrm{OH}^{*\prime}(x, y > 0, t)$) of the combustors centerline eliminates antisymmetric fluctuations, which yields a representation of purely symmetric fluctuations. Vice versa, subtraction eliminates symmetric fluctuation, which yields a representation of purely antisymmetric fluctuations. The integration of these symmetric and antisymmetric fluctuations over the entire flame area provides measures for the global heat release fluctuations induced by symmetric and antisymmetric modes, I'_s and .

The global dynamics of the flame with respect to the PVC and thermoacoustic oscillations are investigated from a spectral analysis of the antisymmetric and symmetric global heat release rate fluctuations. Assuming that the thermoacoustic instability is nominally axisymmetric, the spectrum of the symmetric global heat release rate $I'_s(t)$ points out certain relevant frequencies. Likewise, assuming that the PVC is antisymmetric, the spectrum of the $I'_a(t)$ reveals the response in the flame with respect to the PVC mode. For practical conditions, the flame is typically not perfectly symmetric. This implies that symmetric velocity fluctuations also induce weak antisymmetric heat release rate fluctuations, and antisymmetric velocity fluctuations induce symmetric heat release rate fluctuations, as shown by Acharya et al.[47] Accordingly, traces of the symmetric mode may be found in the antisymmetric-decomposed spectrum and vice versa. The power spectral density (PSD) of the OH*-measurements presented in the results chapter is normalized with the averaged noise level to remove any offset due to different gain settings of the used intensifier.

For a more detailed description of the flame response, the local OH*-signal is decomposed in spatial Fourier modes. These spatial modes are estimated by a point-wise temporal Fourier transform of the OH*-intensity signal, which can be expressed as

$$\widehat{\mathrm{OH}^*}(x, y) = \frac{1}{T}\sum_{t=0}^{T-1} \mathrm{OH}^*(x, y, t) \exp\left(-\frac{i2\pi}{T} ft\right) \qquad (4)$$

Evaluating this equation at the frequency of thermoacoustic oscillations f_{TA} or the PVC frequency f_{PVC} allows to investigate the corresponding structure of the heat release rate fluctuations. The phase of the decomposed spatial modes is adjusted to the respective phase of the maximal global amplitude.

However, the OH*-signal recorded by the camera represents the line-of-sight-integrated values, and an appropriate deconvolution of the data to a planar representation must be conducted. For the symmetric part of the heat release rate, a classic Abel-deconvolution is applied. For the skew symmetric fluctuations induced by the PVC, a tomographic reconstruction technique developed by Moeck et al.[48] was employed. In contrast to conventional tomographic reconstruction techniques, this algorithm only requires one camera. Since the PVC is rotating at a well-defined rate, a phase-resolved sequence of projection images gained from the time-resolved OH*-chemiluminescence snapshots can be used for the tomographic reconstruction.

4. Results

At the beginning of this section, a lock-in study of the isothermal flow inside the combustion chamber is presented, which demonstrates the actuation principal on the basis of SPOD modes and corresponding time coefficients. Thereafter, two reacting cases are considered at

thermoacoustic stable conditions. Starting with a detached M-flame, we actuate the PVC at a frequency slightly lower than the natural frequency, which is considered as a lock-in test. Subsequently, open-loop actuation is applied to an attached V-flame to demonstrate the possibility to excite a PVC for such flame types. In the last and major part, the actuation system is applied to investigate the role of the PVC in a thermoacoustically unstable V-flame. By comparing experimental results from perfectly and partially premixed flames, the dominant interaction mechanisms between the PVC and thermoacoustic instabilities are isolated and discussed.

4.1. Lock-in study at isothermal conditions

The goal of lock-in studies is to demonstrate the principal of the control method. Lock-in describes the state where the dynamics of the PVC are entirely synchronized to the actuation. To reach this synchronization, the actuation amplitude must be increased to a critical value, known as the lock-in amplitude. In a preliminary investigate,[36] the lock-in behavior of the current setup was evaluated based on spectra of pressure measurements. Although these results already demonstrated the working principal of the actuator, the impact of the actuation on the mode shape could not be evaluated. For this purpose, PIV measurements were conducted at the lock-in state to ensure that the natural mode shape of the PVC is not disrupted by the actuation. This is of great importance to unambiguously isolate the impact of the PVC on the combustion properties.

Figure 3 shows the outcome of these PIV measurements. The left side depicts the most energetic SPOD mode (radial velocity component), and the right side depicts the power spectrum of the corresponding mode coefficient. These quantities describe the spatial structure and the dynamic of the PVC, respectively. For better orientation, streamlines derived from the mean flow data are superimposed on the mode shapes. They indicate the inner and outer recirculation zone that is typical for the flow field of a swirl-stabilized combustor. The first row in Figure 3 corresponds to the natural case where the actuator is inactive. The strong fluctuations of the radial velocity component at the jet axis near the inlet indicate the periodic displacement of the jet core which is characteristic for the PVC. The convective vortex pattern in the shear layer between the annular jet and the IRZ indicates the typical downstream propagating single-helical spiral of the PVC. The spectral content of this mode is relatively sharp with a clear peak at the natural Strouhal number.

Once the actuation is applied, an additional peak in the spectrum appears at the actuation frequency, at already very low amplitudes of $C_\mu = 0.05\%$ (see vertical dashed line in Figure 3). Upon increasing the amplitude, this peak becomes dominant, and the natural peak is pulled toward the actuation frequency. This is called frequency pulling and is known as a typical lock-in behavior.[49] At the highest actuation amplitude, the spectral peak has become extremely sharp at significantly higher energy than the natural peak, indicating that the PVC has entirely locked onto the external actuation.

For all actuation amplitudes, the shape of the SPOD modes remains very similar. A trend toward smaller wavelengths is noticeable for higher actuation amplitudes which is due to the fact the locked state corresponds to a higher frequency. Moreover, for the highest actuation amplitude, the mode shape reaches less downstream as in those cases with lower actuation amplitude. This is due to the fact that the strongly forced instabilities undergo nonlinear saturation further upstream compared to the natural case.[50] These effects are expected and of low significance. More importantly, the mode shapes clearly show that the actuator generates the same spatial structure as the natural PVC without causing any artifacts due to the actuation. Above this, the extremely low actuation amplitude of $C_\mu < 0.26\%$ required for lock-in indicates that the actuator is indeed working in a very receptive flow region.

The process of frequency pulling and lock-in can be further investigated by considering the phase difference $\Psi(t)$ between the decomposed pressure signal of the PVC mode ($\hat{p}_1$) and the actuation signal (see e.g. Li and Juniper[51]). Figure 4 shows this quantity as a function of time for the different actuation amplitudes. For the lowest actuation amplitude, the phase decay is nearly constant indicating that the flow does not follow the actuation at all. For higher actuation amplitudes, the phase decay becomes staggered, which means that the flow follows the actuation for the period of time where the phase difference is constant. This kind of behavior is characteristic for frequency pulling. As soon as the flow follows the actuation through the entire time, the state of lock-in is reached. This is characterized by a constant phase difference, as it is the case for the two highest actuation amplitudes.

Last, we address the change of the mean flow field due to the actuation. Figure 5 shows the contour of turbulent kinetic energy $\left(\mathrm{TKE} = \sqrt{\overline{u'^2} + \overline{v'^2}}\right)$ and superimposed mean flow streamlines for the natural and lock-in state. The blue lines indicate zero-mean axial velocity, which indicates the region of reversed flow of IRZ. In both cases, the major turbulent kinetic energy is present near the burner outlet and along the upstream region of the inner shear layer. The comparison of the two cases further shows that the overall

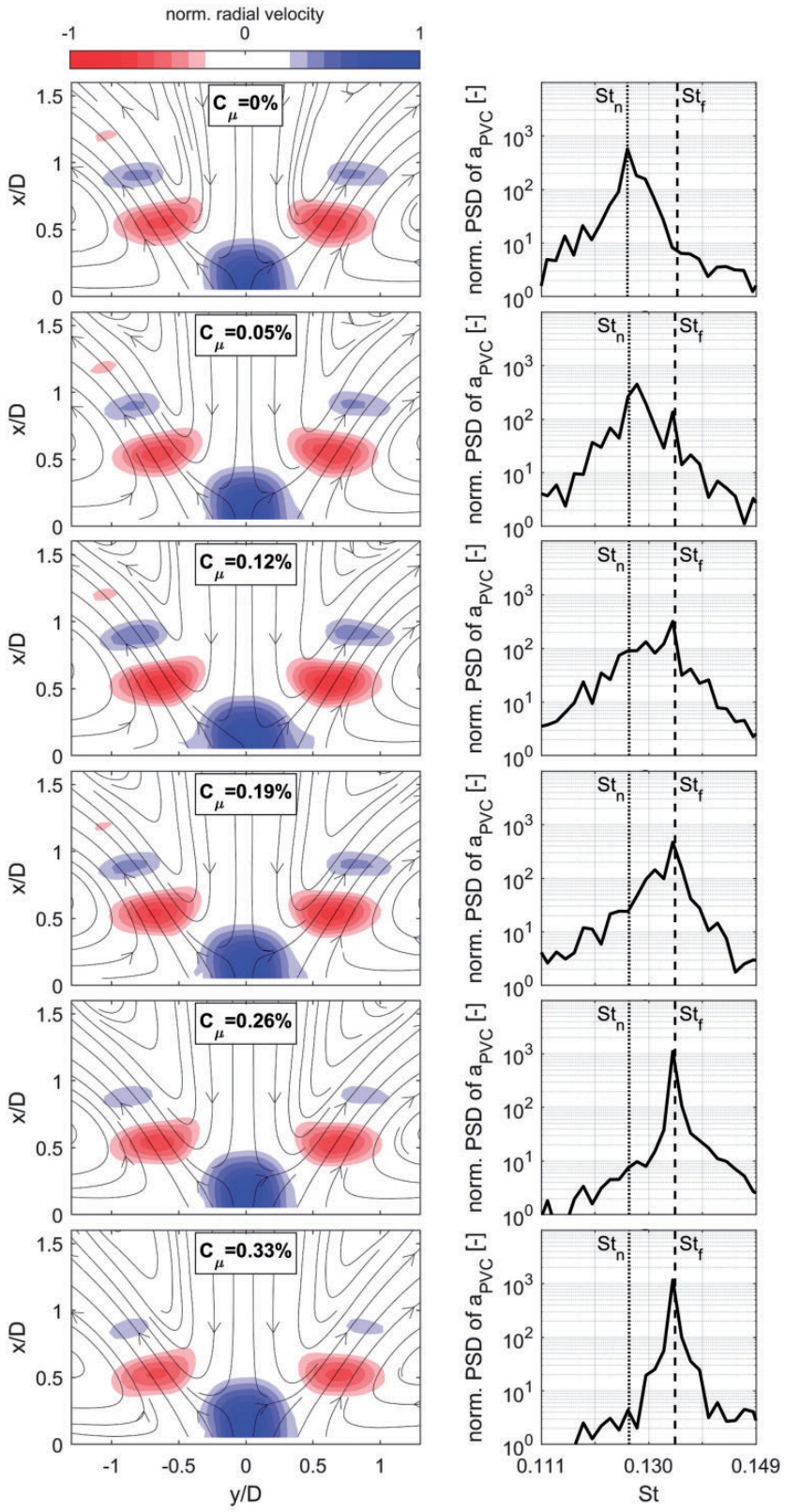

Figure 3. Lock-in study with SPOD modes Φ_{PVC} (left column) and spectra of corresponding time coefficients a_{PVC} (right column). Re = 36,000 Hz ($St_f = 0.135$) and $f_n = 180$ Hz ($St_n = 0.127$).

turbulent kinetic energy is increased due to the actuation, which is due to the strengthening of the PVC fluctuations. It is quite astonishing that the actuation at such low amplitudes causes such an immense increase of turbulent fluctuations (16.5% increase in depicted region). Considering the mean flow, a slight change of the upstream stagnation point of the IRZ is noticeable, which indicates stronger turbulent fluctuations at this location. Nonetheless, the mean flow distortion due to the actuation appears negligible for all cases considering the fact that this is the strongest actuation considered.

From these preliminary results, we can state that the actuator properly locks onto the natural PVC, and it does not cause any artifacts in the flow dynamics. Moreover, lock-in is achieved at very low actuation amplitudes of $C_\mu < 0.26\%$ at comparably high Reynolds numbers. Hence, the actuator appears to be working very efficiently in a region of high receptivity of the PVC.

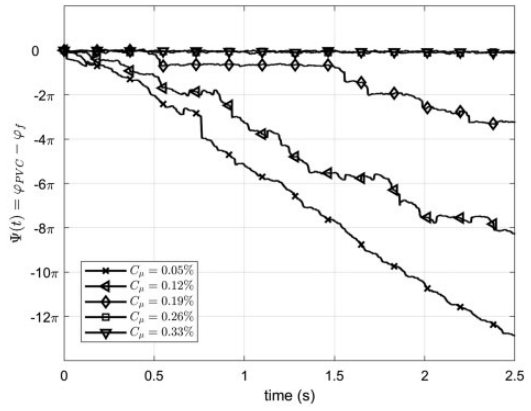

Figure 4. Phase differences $\Psi(t)$ of decomposed pressure signal $\hat{p}_1$ for different actuation amplitudes under isothermal conditions. Re = 36,000, $f_{PVC} = 189$ Hz, and $f_{nat} = 180$ Hz.

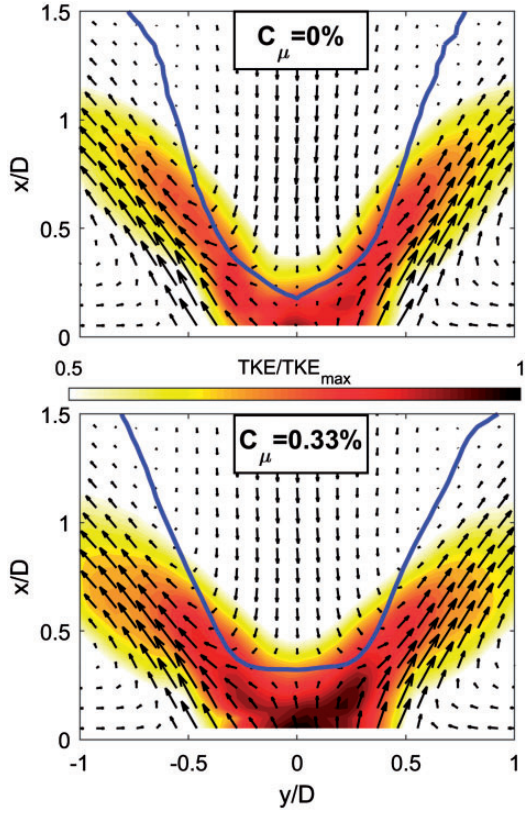

Figure 5. TKE normalized with the maximal value of both plots over the mean flow field (every second measured vector). Top plot: natural (non-actuated) case, bottom plot: actuated case in state of lock-in ($C_\mu = 0.33$) both under isothermal conditions. Re = 36,000, $f_{PVC} = 189$ Hz, and $f_{nat} = 180$ Hz.

4.2. Investigated flame shapes

In this study, two different flame shape types are investigated as depicted in Figure 6. At lean mixtures ($\phi = 0.59$), the flame is detached from the burner outlet and has a characteristic mean shape resembling the letter M, which defines its name, M-flame (left). In richer mixtures in contrast ($\phi = 0.71$), the flame is directly attached to the burner outlet and exhibits a characteristic V-shape. The letter flame therefore is referred to as V-flame in the following (see right-hand side in Figure 6).

Previous studies[3,13] pointed out that a PVC is typically present in M-flames, whereas the V-flame suppresses the PVC. The reason for this suppression is the very strong density stratification induced by the attached V-flame.[3]

The mean flame shapes in Figure 6 reveal a non-symmetric heat release rate distribution of the V-flame; however, the M-flame appears less non-symmetric. This non-symmetry plays an important role

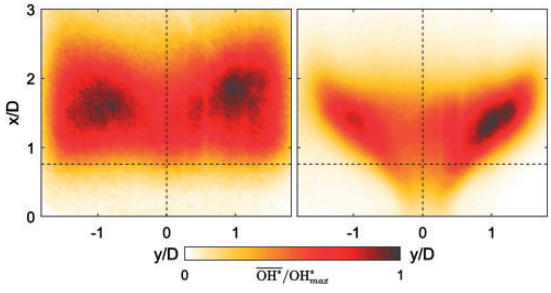

Figure 6. Time-averaged line-of-sight integrated OH*-chemiluminescence of the two basic mean flame shapes which are investigated in this study; M-flame (Re = 30,000 and $\phi = 0.59$) on the left, V-flame (Re = 30,000 and $\phi = 071$) on the right, both perfectly premixed.

in the following investigations. Possible reasons for the asymmetry can be a non-uniform cooling of the burner front plate or a not perfectly symmetric burner design.

4.3. Actuation of the PVC in the M-flame

Starting with the more simple case, we consider a detached M-flame where a PVC naturally occurs. Figure 7 shows the PVC dynamics in the M-flame measured at Reynolds number $\mathrm{Re} = 30,000$ and equivalence ratio $\phi = 0.59$ at perfectly premixed conditions. Figure 7(d) and (e) shows the deconvoluted mean flame shape at non-actuated and actuated conditions. Both resemble the typical M-shape with only minor differences in the flame shape near the wall and flame root position, with the actuated flame appearing somewhat more compact than the non-actuated one.

The pressure spectra shown in Figure 7(a) present the spectral distribution of the first helical mode ($m = 1$). The black line represents natural conditions with the PVC frequency f_{PVC} at around 163 Hz. The peak is relatively broad indicating intrinsic unsteadiness of the PVC limit cycle due to background turbulence. For the actuated flow (red line), the actuation frequency is set to 160 Hz ($St = 0.139$) with an amplitude corresponding to $C_\mu = 0.49\%$, which is above the critical lock-in amplitude. At the actuation frequency, the peak in the actuated pressure spectrum becomes more distinct compared to the natural case. The disappearance of the natural PVC peak indicates the lock-in of the reacting flow to the helical actuation.[36]

Figure 7(b) and (c) shows the spectral distribution of the symmetric and antisymmetric fluctuations $\hat{I}_s$ and $\hat{I}_a$ of the global heat release rate. For the non-actuated case, no dominant peak is visible in the spectrum of $\hat{I}_s$ that would indicate the presence of (symmetric) thermoacoustic modes. However, the spectrum of $\hat{I}_a$ displayed in Figure 7(c) shows the helical PVC mode very distinctly at the same frequency as in the pressure spectrum. When the actuation is turned on, the shape of the symmetric OH*-spectrum remains unchanged, while the antisymmetric OH*-spectrum shows a single distinct peak at the actuation frequency analog to the pressure signals (Figure 7(c)). In connection with the pressure spectrum, which is an indicator for the flow dynamics, it can be concluded that the actuation achieves lock-in of the PVC mode and corresponding heat release rate fluctuations. In the locked state, both pressure and OH*-spectra show a higher PVC amplitude compared to the natural case, which indicates a strengthening of the PVC through the actuation.

Figure 7(f) shows the spatial structure of the oscillation induced by the PVC that can be derived from a vertical slice through the tomographic reconstruction of

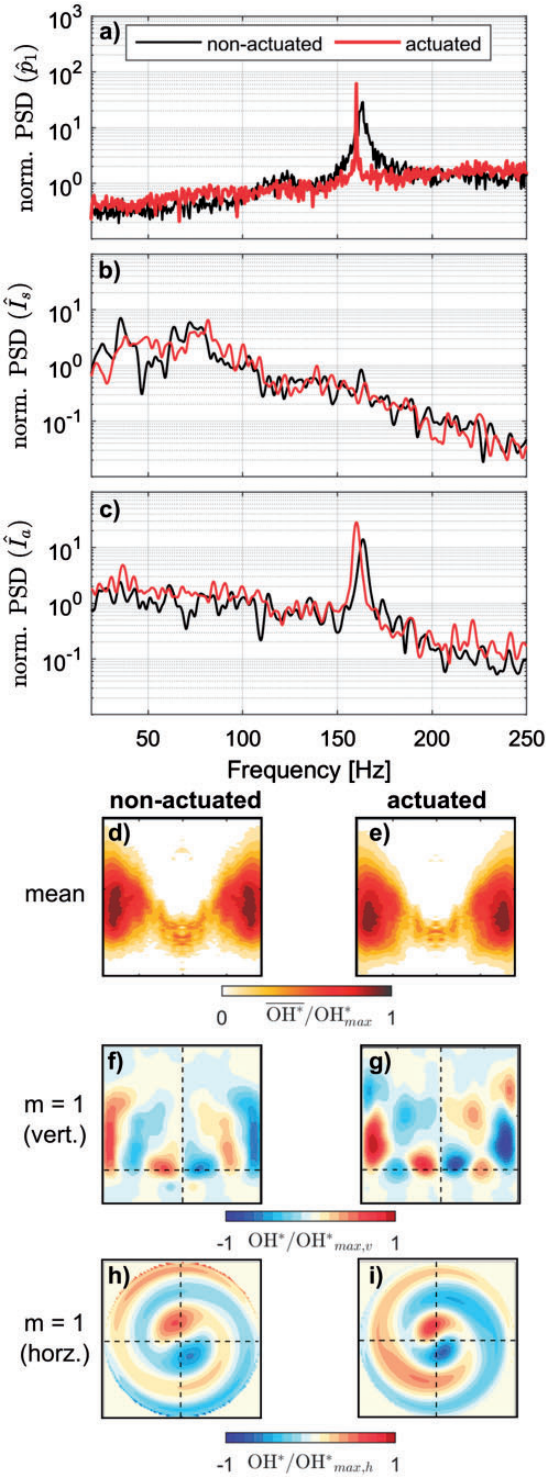

Figure 7. Actuation of M-Flame at $\mathrm{Re} = 30{,}000$ and $\phi = 0.59$, perfectly premixed: (a) spectrum of $m = 1$ pressure mode; spectrum of symmetric (b) and antisymmetric (c) global heat release rate fluctuations; deconvoluted mean OH* of non-actuated (d) and actuated (e) flame; vertical (f, g) and horizontal (h, i) view of the PVC under non-actuated and actuated conditions gained from tomographic reconstruction.

the OH*-signal.[24,48] Accordingly, the PVC acts on the flame especially around the jet axis near the flame root and in the zone of main heat release rate. The fluctuations propagate from the central jet axis, where they are initiated, to the combustor wall. Comparable conclusions can be drawn from the reconstruction at actuated conditions (Figure 7(g)), with the difference that for an actuated PVC, stronger fluctuations near the jet axis upstream and inside the main heat release rate zone appear. In both cases, the regions of strong fluctuations are elongated near the wall due to interaction with the confinement, as already reported by Moeck et al.[24] For the actuated PVC, the heat release fluctuations are stronger in this region indicating enhanced wall-flame interaction. The horizontal slices ($x/D = 0.75$, compare horizontal line in Figure 6) shown in Figure 7(h) and (i) depict a typical shape of a single helical structure, such as the PVC. Furthermore, these plots reveal that the actuated PVC leads to the same flame dynamic structure as for the natural case but the heat release is somewhat more distinct, which is in line with the more distinct pressure peak shown in Figure 7(a). This further demonstrates that the applied actuation indeed actuates a clean PVC structure without generating any additional disturbances of the flame shape.

4.4. Actuation of the PVC in the V-flame

For the V-flame configuration, the equivalence ratio is increased to $\phi = 0.71$ while all other parameters are kept the same as for the previously considered M-flame configuration.

Figure 8(d) shows the deconvoluted mean OH*-intensity illustrating the typical shape of a V-flame. In contrast to the detached M-flame, this flame is attached to the burner outlet. The mean heat release rate for the actuated V-flame (Figure 8(e)) appears more compact, with the region of maximum heat release rate being shifted upstream and inward to the flame root.

Compared to the M-flame, the V-flame does not feature a PVC naturally, which can be seen by the absence of a distinct peak in the decomposed pressure signals in Figure 8(a) for the non-actuated case (black line). The disappearance of the PVC for the V-flame is in line with the previous investigations, showing that the temperature field induced by the flame is suppressing the PVC.[3] The OH*-spectra shown in Figure 8(b) and (c) do not feature any prominent peak for the unforced flame showing no indication for either thermoacoustic instability or a PVC.

When actuation is applied, the $m = 1$ pressure spectrum depicted in Figure 8(a) shows a clear peak at the actuation frequency of 160 Hz ($St = 0.139$, $C_\mu = 0.49\%$). This peak has a similar amplitude as for the forced M-flame configuration, providing first

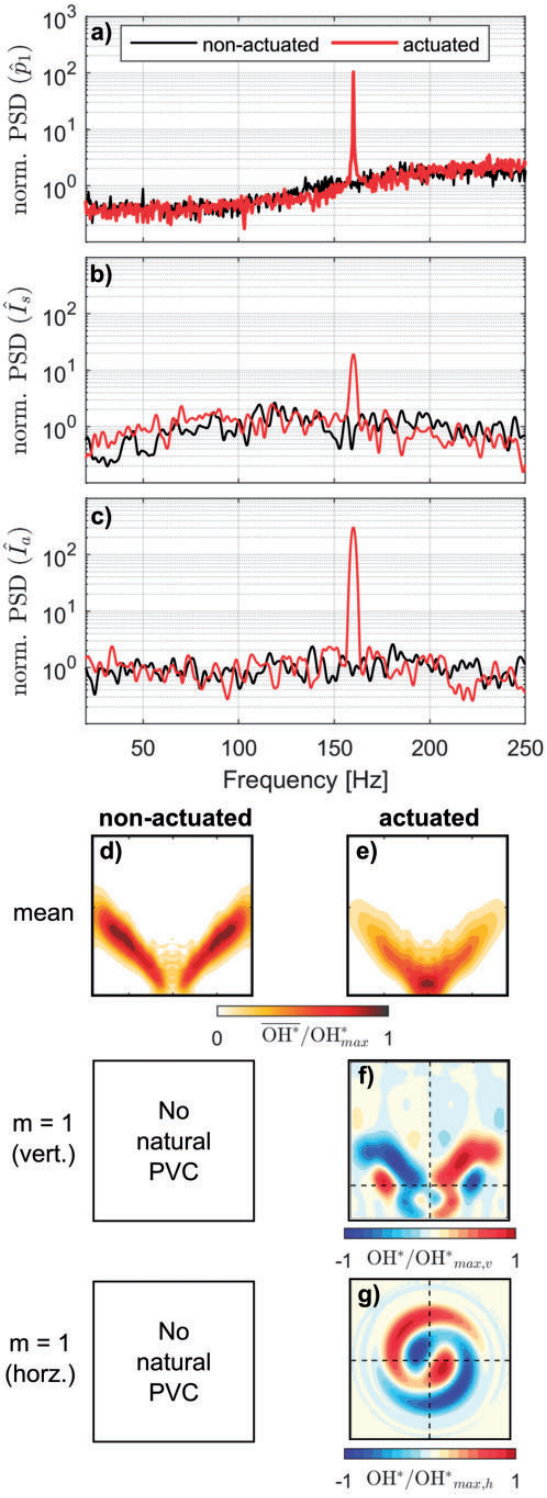

Figure 8. Actuation of V-flame at Re = 30,000 and $\phi = 0.71$, perfectly premixed: (a) spectrum of $m = 1$ pressure mode; spectrum of symmetric (b) and antisymmetric (c) global heat release rate fluctuations; deconvoluted mean OH* of non-actuated (d) and actuated (e) flame; vertical (f) and horizontal (g) view of the PVC under non-actuated and actuated conditions gained from tomographic reconstruction.

indication that the actuation is actually triggering a PVC instability.

Considering the symmetric OH*-spectrum shown in Figure 7(b), we observe a small peak at the actuation amplitude. This is surprising as it is generally expected that the antisymmetric actuation does not cause symmetric heat release rate fluctuations. This is most probably due to the fact that the V-flame is not perfectly symmetric (compare Figure 6). This is in accordance with the work by Acharya et al.,[47] who found that an axisymmetric excitation field can excite helical flame disturbances in non-axisymmetric reacting swirling flows and vice versa.

Considering the flame dynamic structures shown in Figure 7(f) and (h), no descriptive reconstructed mode can be shown for the non-actuated V-flame because it does not feature any dominant (PVC) dynamics. For the actuated case, the vertical slice through the reconstructed helical structure shows a distinct mode induced by the actuated PVC, which is present along the flame front (Figure 8(f)). The intensity appears to be considerably higher along the flame arms compared to the region of the flame root. Obviously, the fluctuations induced near the flame root seem to grow considerably in spatial extend as well as intensity when traveling downstream along the flame front. The horizontal slice shown in Figure 8(g) shows the typical helical shape of the emerging PVC in the region of the flame root.

The discussion of Figure 8(e) to (g) reveals plausible and considerable interactions between the PVC and the V-flame, which have not been observed before in such a controlled manner.[12] However, the selection of the actuation frequency and mode for the V-flame is based on the hydrodynamic instability of the M-flame, which requires some additional explanations. A previous study by Oberleithner et al.[3] revealed that the reason for the suppression of the PVC in the V-flame is not the difference in the mean flow but the difference in the density stratification. Accordingly, it has been concluded that the general hydrodynamic instability is very similar for both types of flames. Therefore, we decided to actuate the V-flame near the frequency of the natural PVC of the M-flame.

The validity of the current control scheme is further supported by the similarity of the response of the M- and V-flame to PVC actuation. The tomographic reconstruction of the helical flame fluctuations presented in Figures 7 and 8 reveals flame fluctuations that start to rise near the center jet axis, where the wavemaker of the PVC is typically found and grows along the flame front. These considerations lead to the conclusion that the actuated structures are not describing a helical response of the shear layers to the actuation but an actuated PVC.

Hence, the V-flame configuration is an appropriate case to study the direct influence of PVC on the combustion processes as it can be controlled freely from zero to large amplitudes, which is not the case for the M-flame where the PVC occurs naturally. In the following, the V-flame configuration is used to study the influence of the PVC on thermoacoustic oscillations.

4.5. Interaction of a thermoacoustic instability and the PVC in a perfectly premixed V-flame

In the literature, different interaction mechanisms between axisymmetric thermoacoustic and single-helical PVC modes are described. We address the following three mechanisms in this study:

- Frederick et al.[19] showed in their analysis that the PVC leads to a thickening of the shear layers and, hence, reduces the growth rate of the Kelvin–Helmholtz instability, which is also known as a key driver for thermoacoustic instability.[52]
- Steinberg et al.[14] associate the interaction of single helical and thermoacoustic modes with stretching and contraction of the PVC by the thermoacoustic mode. They showed that the heat release fluctuations are aligned to the interaction mode, which causes asymmetric radially detached flame patterns.
- Moeck et al.[24] concluded that the rise of an interaction mode is caused by nonlinear processes in the flame dynamics since they could not detect it in their velocity measurements under self-excited conditions.

To investigate the interaction between PVC and thermoacoustic modes, the PVC actuation is applied to a perfectly premixed flame featuring self-excited thermoacoustic oscillations at $\phi = 0.73$ and $\mathrm{Re} = 26{,}000$. The actuation frequency is set to the natural frequency of the PVC at isothermal conditions of $f_{\mathrm{PVC}} = 138$ Hz ($St = 0.14$), which is close to the PVC frequency of the M-flame at $\phi = 0.59$.

In Figure 9, the spectra of the decomposed pressure signals $\hat{p}_0$ and $\hat{p}_1$ as well as the corresponding OH*-signals $\hat{I}_s$ and $\hat{I}_a$ are compared for non-actuated and actuated conditions. The actuation amplitude is set to $C_\mu = 0.65\%$, which is the equivalent lock-in amplitude of the M-flame.

The non-actuated pressure spectrum of mode $m = 0$ shown in black in Figure 9(a) reveals a distinct peak of the dominant thermoacoustic mode at $f_{\mathrm{TA}} = 120$ Hz and minor peaks of the subharmonic and first harmonic at 60 and 240 Hz. Above this, a peak is present at 180 Hz, which represents the interaction of the fundamental and subharmonic oscillation. The corresponding spectrum of the symmetric OH*-signal in Figure 9(b) reveals the fundamental and first harmonic at the

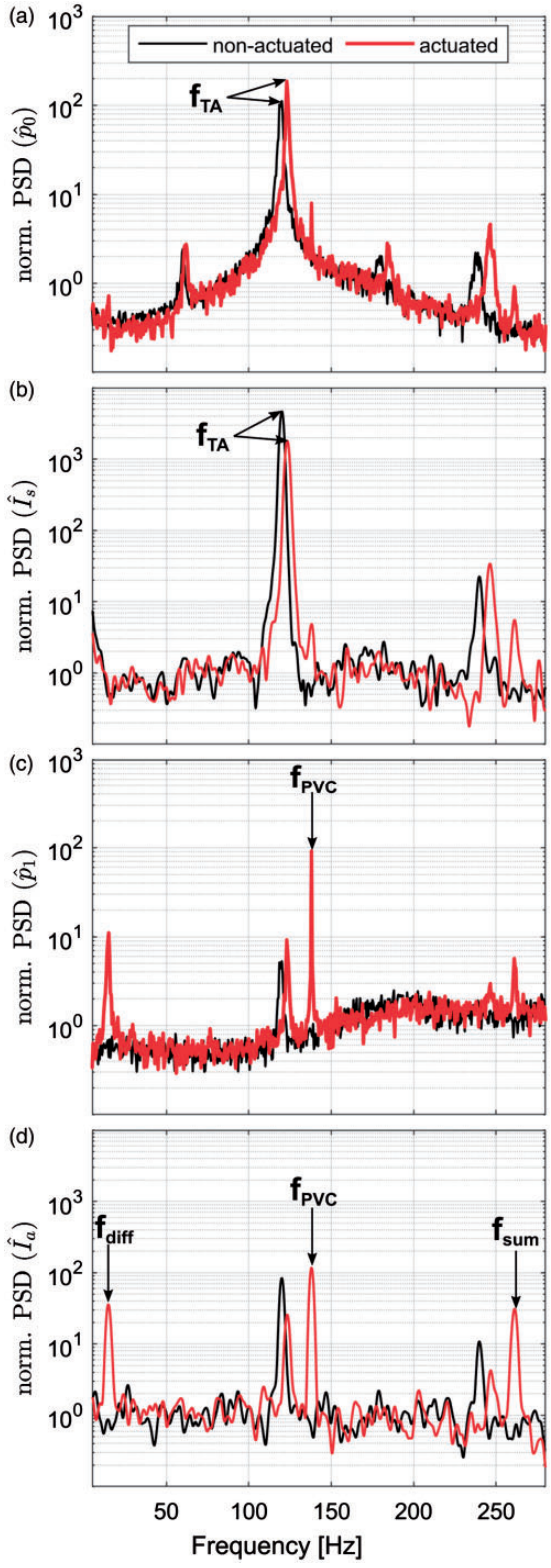

Figure 9. Effect of PVC actuation on thermoacoustic oscillations of V-flame at Re = 26,000, $\phi = 0.73$, and $C_\mu = 0.65\%$ (perfectly premixed): spectra of $m = 0$ (a) and $m = 1$ (c) pressure mode; spectra of symmetric (b) and antisymmetric (d) global heat release rate fluctuations.

same frequency as the pressure spectrum. On the contrary, the subharmonic and its interaction with the fundamental frequency are not visible in the OH*-signal. All these peaks describe the dynamics of the thermoacoustic oscillation under non-actuated conditions, whereas the subharmonic oscillation and its interaction with the fundamental are only a pressure phenomenon indicating possibly a subharmonic resonance of the shear layer.

The pressure spectrum of the helical mode in Figure 9(c) shows a small peak at the fundamental thermoacoustic frequency. This small peak is unexpected when considering axisymmetric perturbations of an axisymmetric flame. However, as discussed above, the mean flame shape of the V-flame is not perfectly axisymmetric. Therefore, the nominally axisymmetric thermoacoustic instability may indeed cause antisymmetric flame disturbances. Likewise, the antisymmetric PVC may induce symmetric (global) flame fluctuations.[47]

Compared to the pressure spectrum, the spectrum of the antisymmetric OH*-signal reveals the fundamental frequency of the thermoacoustic mode more distinctly together with the first harmonic (compare Figure 9(d)). This observation suggests that the symmetric thermoacoustic oscillations are rather affecting the dynamics of the antisymmetric flame component than the first helical pressure mode.

Considering the actuated case, both the asymmetric OH* spectrum and the $m = 1$ pressure spectrum show a clear peak at the actuation frequency (Figure 9). Hence, despite the pulsations induced by the thermoacoustic instability, the PVC actuation is effective. The spectra further show that the actuation of the PVC causes a slight shift of the thermoacoustic frequencies toward higher values. It is further noticeable that the PVC actuation causes fluctuation in the symmetric OH* spectrum, which is most probably due to the asymmetry mean flame shape.

Because of the presence of two dominant modes, PVC and thermoacoustic mode, nonlinear interactions take place between these modes. These interactions cause peaks in the spectrum at frequencies corresponding to sums or differences between the frequency of the PVC and the thermoacoustic mode. Such an interaction peak is present at $f_{\text{diff}} = f_{\text{PVC}} - f_{\text{TA}} = 15$ Hz and has been observed and analyzed in other configurations as well.[14,24] For example, Moeck et al.[24] also found interaction peaks at a frequency f_{sum} equal to the sum of f_{TA} and f_{PVC} under self-excited conditions that appeared only in the velocity signals. In the present study, such an interaction peak is present in the pressure spectrum of the first helical as well as in the antisymmetric OH* spectrum at $f_{\text{sum}} = f_{\text{PVC}} + f_{\text{TA}} = 258$ Hz, as indicated in Figure 9(d). These interaction modes are mainly

antisymmetric, which is in line with the observations of Steinberg et al.[14] and Moeck et al.[24] Therefore, these peaks are comparably larger in the antisymmetric spectra in Figure 9(c) and (d). The symmetric spectra reveal the high frequency interaction peak quite clearly; however, the low frequency interaction peak is only marginal in the spectra of the symmetric pressure and OH* signals. This leads to the conclusion that the interaction modes primarily have a helical and antisymmetric structure.

In Figure 10(a) and (b), the mean shapes of the non-actuated and actuated flames are represented. Accordingly, the actuation shifts the zone of major heat release rate from the flame tip to the flame root, whereby the whole flame becomes more compact.

Figure 10(c) and (d) reveals the structure of heat release rate fluctuations for the thermoacoustic mode ($m = 0$) that were reconstructed via point-wise Fourier transform and subsequent Abel deconvolution. The horizontal representations (e and f) are computed by rotating the vertical representation by 180° and extracting one horizontal slice at $x/D = 0.75$ (compare horizontal dotted line in Figure 10(c) and (d)). The vertical representation of mode $m = 0$ represents the axisymmetric thermoacoustic oscillations traveling along the flame. The contours are normalized by the maximal absolute value, which allows for a clear representation of the spatial shape. The vertical and corresponding horizontal shapes are slightly changed by the actuation due to the change of the mean flame. Accordingly, the spots of high fluctuation amplitude around the jet center axis in the non-actuated flame are dispersed by the PVC actuation. This leads to a broader area of constant fluctuation amplitude around the jet center axis at the flame root in the actuated case. The amplitude reduction of the strongly fluctuating spots is revealed by the horizontal representations as well. Nonetheless, in both flames, the strongest fluctuations can be seen at the flame tip.

In Figure 10(g) and (h), vertical and horizontal slices through the reconstructed OH*-fluctuations induced by the PVC are given only for the actuated flame. These plots are normalized by the maximal absolute value of the respective slice. The vertical shape of mode $m = 1$ is very similar to that in the actuated thermoacoustically stable V-flame shown in Figure 8. The major difference is the elevated fluctuation near the jet axis for the unstable flame. A reason for that can be the difference in the mean flame shape due to the thermoacoustic mode. The horizontal slice in Figure 10(h looks also very similar to the actuated stable case, revealing the typical helical shape of the PVC. This comparison shows that the flame response to the PVC actuation is qualitatively the same for the thermoacoustically stable and unstable V-flame.

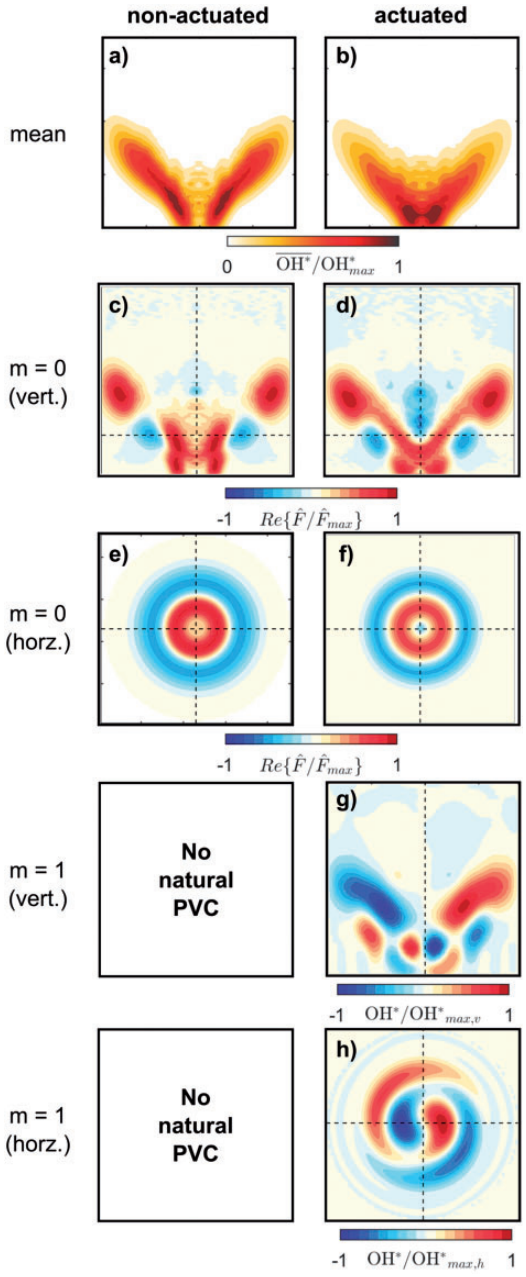

Figure 10. Effect of actuation on thermoacoustic and PVC mode shapes of V-flame at Re = 26,000 and $\phi = 0.73$ (perfectly premixed): deconvoluted mean OH* of non-actuated (a) and actuated (b) flame; thermoacoustic mode shape (Fourier mode) under natural (c) and actuated (d) conditions; horizontal view of thermoacoustic mode at $x/D = 0.75$ reconstructed from Fourier mode (e, f); vertical (g) and horizontal (h) view of the PVC under non-actuated and actuated conditions gained from tomographic reconstruction.

The various nonlinear interaction modes discussed above do not explain the change of the fundamental frequency of the thermoacoustic oscillations with applied actuation. To gain a deeper insight into this mechanisms, a parameter study was conducted where

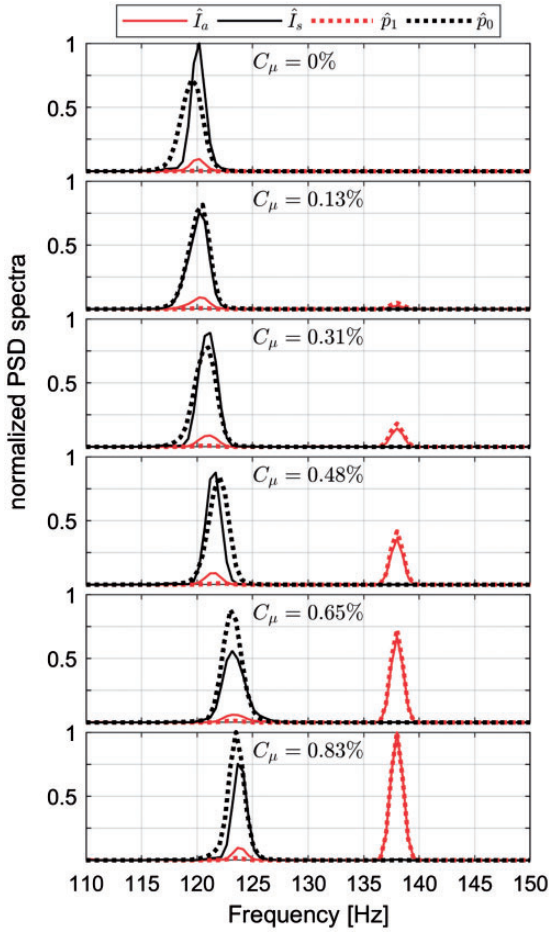

Figure 11. Spectra of global symmetric $\hat{I}_s$ (black solid) and antisymmetric $\hat{I}_a$ (red solid) OH*-signal as well as decomposed pressure spectra of mode $m = 0$ ($\hat{p}_0$, black dotted) and mode $m = 1$ ($\hat{p}_1$, red dotted) for different actuation amplitudes under thermoacoustically unstable conditions at Re = 26,000, $\phi = 0.73$, and $f_{PVC} = 138$ Hz.

the PVC actuation amplitude was step-wise increased at a constant actuation frequency of $f_{PVC} = 138$ Hz. The results are depicted in Figure 11 showing a zoom-in of the spectra of symmetric and anti-symmetric OH* fluctuations as well as the axisymmetric and helical pressure spectra for different actuation amplitudes. These spectra are generated by applying the Welch's overlapped segment averaging spectral estimation (*pwelch* Matlab command) with a segment length of sampling rate/1 s and an overlap of 50%. To allow relative comparisons, all values are normalized with respect to an overall maximum value.

For the non-actuated case (top image of Figure 11), the symmetric OH*-spectrum reveals the fundamental thermoacoustic frequency of 120 Hz. Likewise, the symmetric pressure spectrum shows a peak at this frequency. The antisymmetric OH*-spectrum also shows considerable spectral content at the frequency of the thermoacoustic instability, which is due to the slight asymmetries of the mean flame shape. These antisymmetric flame fluctuations are two magnitudes weaker than the symmetric flame fluctuations induced by the thermoacoustic mode (compare Figure 9). Apparently, the antisymmetric flame fluctuations are not strong enough to generate a prominent peak at this frequency in the normalized pressure spectrum of $\hat{p}_1$ in Figure 11.

For the actuated cases (rows two to six of Figure 11), the actuation frequency f_{PVC} is set to 138 Hz, and the actuation amplitude is step-wise increased. Comparing the amplitudes of the symmetric OH*-signal with the pressure signal of mode $m = 0$ for increasing actuation amplitude, different trends can be seen. Whereas the amplitude of the OH*-signal has its maximum at a low actuation amplitude, the pressure signal reaches its maximum at the highest actuation amplitude. Therefore, no clear trend can be drawn regarding the impact of the PVC actuation on the amplitude of the thermoacoustic mode. What is more obvious is the shift of the frequency of the thermoacoustic oscillations to higher values. From the natural frequency of 120 Hz, a gradual frequency shift toward 124 Hz takes place with increasing actuation amplitude. These results suggest that the actuation of the PVC has only minor effect on the amplitude of the thermoacoustic oscillations, but it shows an impact on the frequency of the thermoacoustic oscillations. Consequently, the results show as well that the thermoacoustic feedback cycle is not disrupted by the PVC, as the amplitude of the thermoacoustic oscillations is not affected considerably by the PVC actuation.

Frederick et al.[53] have proposed a mechanism that describes how the PVC may suppress the thermoacoustic oscillations in perfectly premixed flames. The authors suggest that the coherent Reynolds stresses induced by the PVC may lead to a thickening of the shear layers that is sufficient to significantly reduce the growth rates of the axisymmetric Kelvin–Helmholtz instability, which in turn leads to the reduction of the thermoacoustic oscillations.[52,54] To investigate on this mechanism, Figure 12 shows the the amplitude of thermoacoustic pressure oscillations against the actuation amplitude for a number of different actuation frequencies. To estimate the amplitude of the thermoacoustic oscillations (TA amplitude), the corresponding PSD spectrum of the decomposed pressure signal of mode $m = 0$ is integrated around the related peak. Finally, the amplitude is equal to the square root of this integral value. The resulting data shows only a very slight dependence of these two quantities, which demonstrates that the proposed mechanism is irrelevant for this flame. Moreover, a detailed investigation of the mean flow field measured at isothermal conditions shows that the shear layer thickness is only marginally affected by the PVC actuation (not

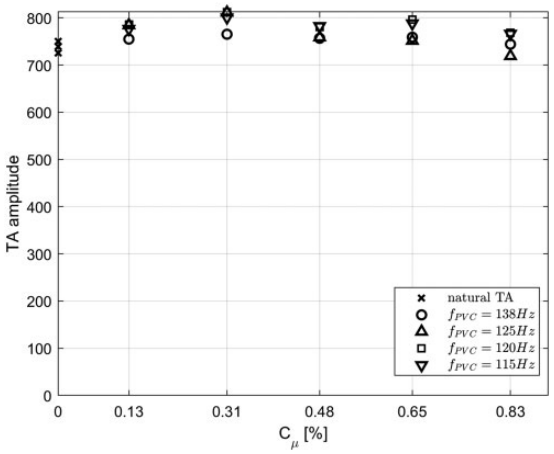

Figure 12. Amplitudes of thermoacoustic mode from integrated pressure spectrum for different actuation frequencies (f_{PVC}) and amplitudes (C_μ) at Re = 26,000 and $\phi = 0.73$–0.74.

shown here for brevity). Hence we conclude that the modification of the mean flow field through the PVC and the indirect influence on the axisymmetric Kelvin–Helmholtz instability are of minor importance for this flame.

Figure 11, however, shows a clear impact of the PVC actuation on the frequency of the thermoacoustic mode. A possible reason for this behavior might be the change of the convective time-delays within the thermoacoustic feedback loop, which might be induced by the change of the mean flame shape. The thermoacoustic feedback cycle is driven by the phase difference between the heat release rate perturbations and the pressure perturbations in the combustion chamber. These perturbations in itself are driven by the time delay between velocity perturbations at the combustor inlet and subsequent heat release rate perturbations in the flame downstream. As shown by Silva and Polifke,[55] this time delay may directly influence the thermoacoustic frequency.

To further investigate this mechanism, the mean flame position is estimated by the center of mass (COM) of one half of the deconvoluted mean OH*-field, reading[39]

$$\mathrm{COM}_y = \frac{\overline{\int \overline{\mathrm{OH}^*}(x,y)x\,\mathrm{d}x}}{\overline{\int \overline{\mathrm{OH}^*}(x,y)\,\mathrm{d}x}}; \qquad \mathrm{COM}_x = \frac{\overline{\int \overline{\mathrm{OH}^*}(x,y)y\,\mathrm{d}y}}{\overline{\int \overline{\mathrm{OH}^*}(x,y)\,\mathrm{d}y}} \tag{5}$$

The estimated flame positions are shown in Figure 13(a) for different actuation frequencies and amplitudes. It illustrates the gradual movement of the mean flame in the (x,y)-plane induced by the PVC actuation. The data shows a clear trend for all considered actuation frequencies. Accordingly, the flame moves

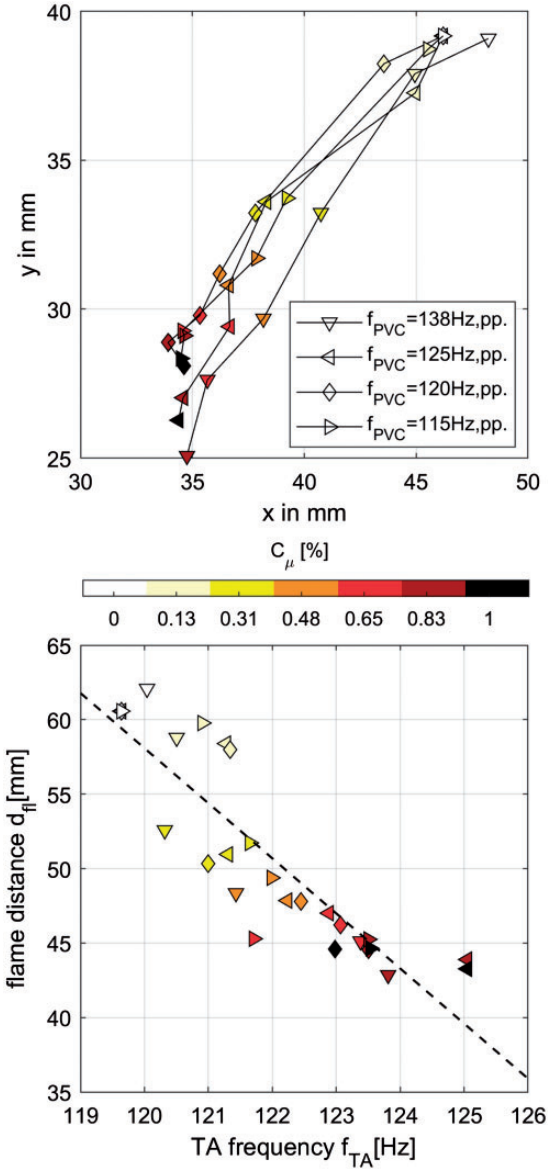

Figure 13. (a) Axial (x) and radial (y) coordinates of estimated flame position for different actuation frequencies (f_{PVC}) and amplitudes (C_μ) at Re = 26,000 and $\phi = 0.73$–0.74; (b) regression of flame distance $d_{fl} = \sqrt{x^2 + y^2}$ over thermoacoustic frequency f_{TA} for the same operating conditions as in (a).

upstream toward the burner outlet and in radial direction toward the center axis for increasing actuation amplitude. This results in a more compact flame with major heat release near the center axis, as shown for example in Figure 10. A possible reason for the upstream movement of the flame is an increase in turbulent burning velocity induced by the PVC actuation. Due to the actuation, the turbulent fluctuations are enhanced near the burner outlet, which increases the wrinkling of the flame front (compare Figure 5). The enhanced wrinkling increases the turbulent burning velocity, which causes flame anchoring more upstream

inside the inner shear layer where the increased burning velocity matches the higher flow velocity.

The coordinates of the flame position in the (x,y)-plane are condensed to one quantity by calculating the distance of the flame $d_{\mathrm{fl}} = \sqrt{x^2 + y^2}$ to the center of the burner outlet. This flame distance is plotted over the corresponding dominating thermoacoustic oscillation frequency f_{TA} in Figure 13(b) for a number of actuation frequencies and amplitudes. The figure reveals a clear correlation between the thermoacoustic frequency and the flame distance as well as the PVC amplitude.

The distance of the flame (Figure 13(b)) can be used to estimate the convective time delay from the burner front plate to the flame using a bulk velocity estimated at 11.57 m/s based on the geometry and the fuel-air mass flow. Accordingly, the time delay τ is equal to 5.2 ms for the non-actuated flame. Together with the period duration of $T = 1/f_{\mathrm{TA}}$, the ratio is $\tau/\mathrm{T} = 0.63$. For the actuated cases with maximal actuation amplitude, the ratio τ/T is estimated at 0.47 equivalently to the non-actuated case. The difference of 16% causes a significant phase shift between the heat release and pressure fluctuations which may lead to a slight increase of the frequency of the thermoacoustic oscillations.[55–57] The very recent work by Silva and Polifke[55] provides a theoretical framework, which supports the increase in frequency induced by decreasing time delay.

In conclusion, the results show that the PVC actuation causes a more compact flame with the major heat release shifted upstream. This leads to smaller convective time-lags and changes in the phase relation between heat release rate and pressure in a way that higher thermoacoustic frequencies occur.

4.6. Interaction of a thermoacoustic instability and the PVC in a partially premixed V-flame

In this section, we consider a partially premixed V-shaped flame where fuel injection is applied at the swirler. For this condition, equivalence ratio fluctuations generated at the fuel injector may play a key role in the thermoacoustic feedback cycle.[58–60] The global parameters are set to $\mathrm{Re} = 22{,}000$ and $\phi = 0.71$. As in the section before, we first consider the spectra of global OH* and decomposed pressure signal for the non-actuated flame and the flame actuated at an amplitude of $C_\mu = 0.94$ % (Figure 14). Without actuation, a dominant oscillation is clearly detected in the global OH*- and symmetric pressure spectrum, as shown in Figure 14(a) and (b), with the fundamental frequency at $f = 76.5$ Hz. The strength of the peak and the existence of higher harmonics indicate a strong thermoacoustic oscillation. Similar to the perfectly premixed flames discussed earlier, the partially premixed flame is not

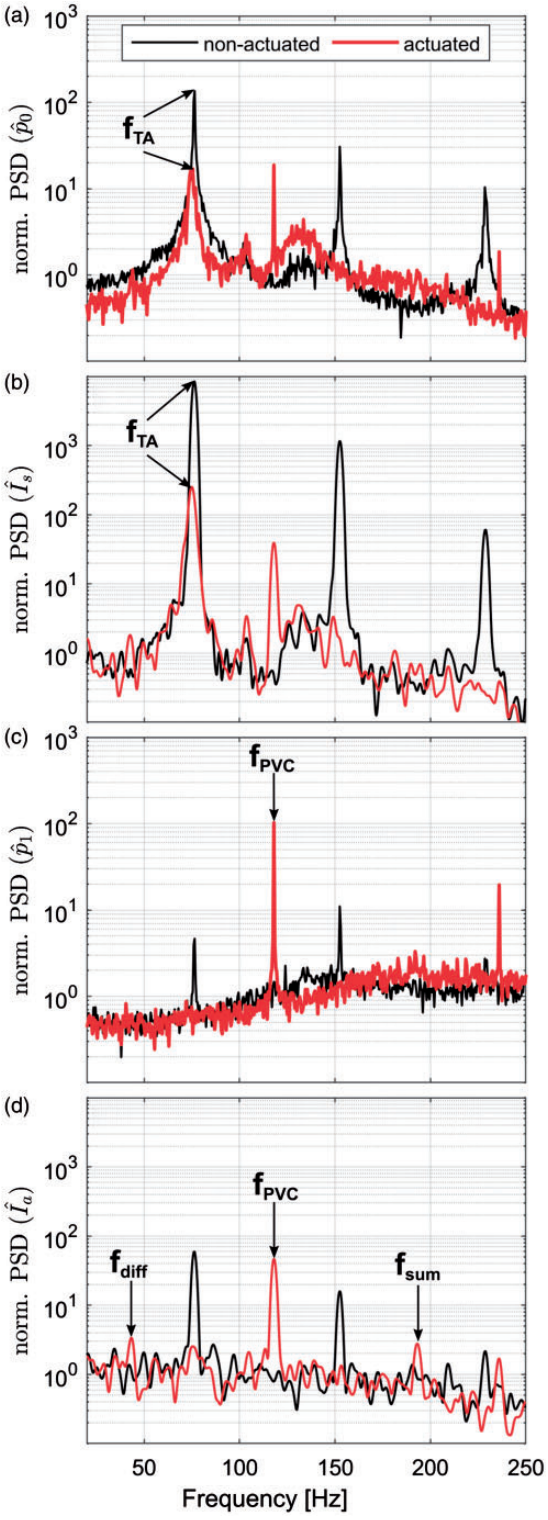

Figure 14. Effect of PVC actuation on thermoacoustic oscillations of V-flame at $\mathrm{Re} = 22{,}000$, $\phi = 0.71$ (partially premixed): spectrum of $m = 0$ (a) and $m = 1$ (c) pressure mode; spectrum of symmetric (b) and antisymmetric (d) global heat release rate fluctuations.

perfectly symmetric, which explains the distinct contribution of the thermoacoustic oscillation at 76.5 and 153 Hz to the antisymmetric OH*-signal shown in Figure 14(d). However, compared to the symmetric OH*-spectrum, the amplitudes are two magnitudes lower. The pressure spectrum of mode $m=1$ contains only marginal peaks at the thermoacoustic frequencies, which can be seen in Figure 14(c). This underlines the fact that the antisymmetric heat release fluctuations found at the non-actuated state are not driven by a PVC, but by the asymmetry of the flame shape.

Considering the actuated case next (red lines in Figure 14), the $m=1$ pressure spectrum does not show any peaks at the frequencies of the thermoacoustic oscillation. Instead, the PVC actuation generates a dominant peak at the corresponding frequency of 118 Hz and a considerable lower one at the first harmonic at 236 Hz. Accordingly, the actuation achieves to excite a PVC even at the presence of strong thermoacoustic oscillations that occur under partially premixed conditions.

The most remarkable effect of the actuation is the considerable suppression of the thermoacoustic oscillations. This can be seen in the spectrum of the symmetric (global) OH*-spectrum, and the pressure spectrum of the symmetric mode is shown in Figure 14(a) and (b). Accordingly, the oscillations are reduced by one order of magnitude at the fundamental frequency, and the peaks at the higher harmonics are completely suppressed. The $m=0$ pressure spectrum further shows a new peak at the PVC frequency at a similar amplitude as the remaining thermoacoustic oscillation. This slight coupling between the $m=1$ actuation and the $m=0$ oscillations is most likely due to the asymmetries of the mean flame shape.

The PVC may also influence the thermoacoustic mode through a direct nonlinear interaction, as shown earlier for the perfectly premixed flame. Corresponding characteristic peaks in the antisymmetric OH*-spectrum shown in Figure 14(d) are indicative for such interactions, such as the low-frequency interaction mode oscillates at $f_{\mathrm{diff}}=43$ Hz, which corresponds exactly to the difference of the actuation frequency $f_{\mathrm{PVC}}=118$ Hz and the frequency of the thermoacoustic mode $f_{\mathrm{TA}}=75$ Hz. The high-frequency mode at $f_{\mathrm{sum}}=193$ Hz corresponds to the sum of the two frequencies. It is considerably lower than for perfectly premixed flames due to the strong damping of the thermoacoustic mode (compare Figure 9(d)).

The mean flame shape of the non-actuated and actuated cases is shown in Figure 15(a) and (b), respectively. The actuated flame exhibits distinct differences to the non-actuated flame especially concerning the concentrated shape of the zone of maximum OH*-intensity at the flame root. This difference was already observed for perfectly premixed conditions (Figure 8(b)); however, at technically premixed conditions, the flame appears even more compact, indicating better mixing at the flame root due to the PVC actuation.

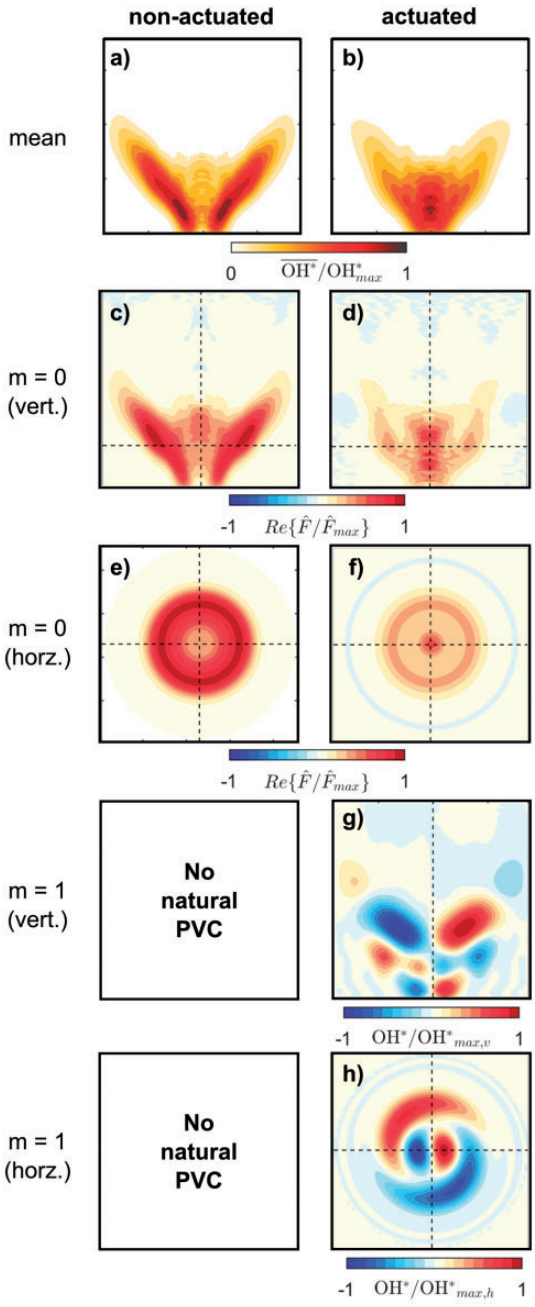

Figure 15. Effect of actuation on thermoacoustic and PVC mode shapes of V-flame at Re = 22,000 and $\phi=0.71$ (partially premixed): deconvoluted mean OH* of non-actuated (a) and actuated (b) flame; thermoacoustic mode shape (Fourier mode) under natural (c) and actuated (d) conditions; horizontal view of thermoacoustic mode at $x/D=0.75$ reconstructed from Fourier mode (e, f); vertical (g) and horizontal (h) view of the PVC under non-actuated and actuated conditions gained from tomographic reconstruction.

Figure 15(c) shows the symmetric heat release rate fluctuations at the fundamental frequency of the thermoacoustic oscillation. It indicates that the flame expands downstream in axial and radial direction during one cycle before it collapses and moves upstream again to repeat this periodic motion. For the actuated case, the spatial expansion and the amplitude of the thermoacoustic mode are clearly reduced (Figure 15(d)). This implies that the considerably damped remaining heat release rate fluctuations for the actuated case are now occurring near the jet center and no longer at the flame tip. The horizontal slices shown in Figure 15(e) and (f) underline this effect.

Finally, Figure 15(g) and (h) shows the reconstructed heat release rate induced by the PVC actuation. The comparison with the perfectly premixed case shown in Figure 10(g) and (h) reveals that the applied actuation is indeed causing a PVC-like structure in the flame response. Slight differences appear which can be attributed to the higher compactness of the flame at partially premixed conditions.

The present experiment reveals a significant suppression of the thermoacoustic instability through the actuation of the PVC. An explanation for the suppression of the thermoacoustic instability by the PVC is given by Frederick et al.,[19] as described above. However, our experiments conducted at perfectly premixed conditions for different actuation frequencies and amplitudes (compare Figures 10 and 11) do not support this explanation. Since the burner is operated at partially premixed conditions, one possible reason for the suppression is the improved mixing caused by the PVC actuation upstream of the flame. The improved mixing reduces the equivalence ratio fluctuations generated at the fuel injectors, which are known to be key driver for thermoacoustic oscillations.[58–60] As for the perfectly premixed flame, the change in convective time delay due to the upstream shift of the flame may influence the thermoacoustic oscillation in the partially premixed flame as well. For the partially premixed case, the time delay τ is considerably higher because the mixing tube length from the injector to the burner outlet needs to be induced as well. Therefore, the time delay is estimated at 15.9 ms for the non-actuated case, which leads to $\tau/\mathrm{T} = 1.22$, because of the low frequency of the thermoacoustic oscillations at 76.5 Hz. For the actuated case with maximal damping of the thermoacoustic oscillation, the time delay is reduced to 14.2 ms and $\tau/\mathrm{T} = 1.09$. The difference of 13% is comparable to that for the perfectly premixed flame. However, different from the perfectly premixed flame, the PVC actuation appears to induce a phase shift between heat release and pressure that is sufficient to push the system dynamics from an unstable state to more stable thermoacoustic conditions. Although the relative difference in time delay is equal for the perfectly premixed case, the amplitude of the thermoacoustic oscillations is not affected considerably. Therefore, we

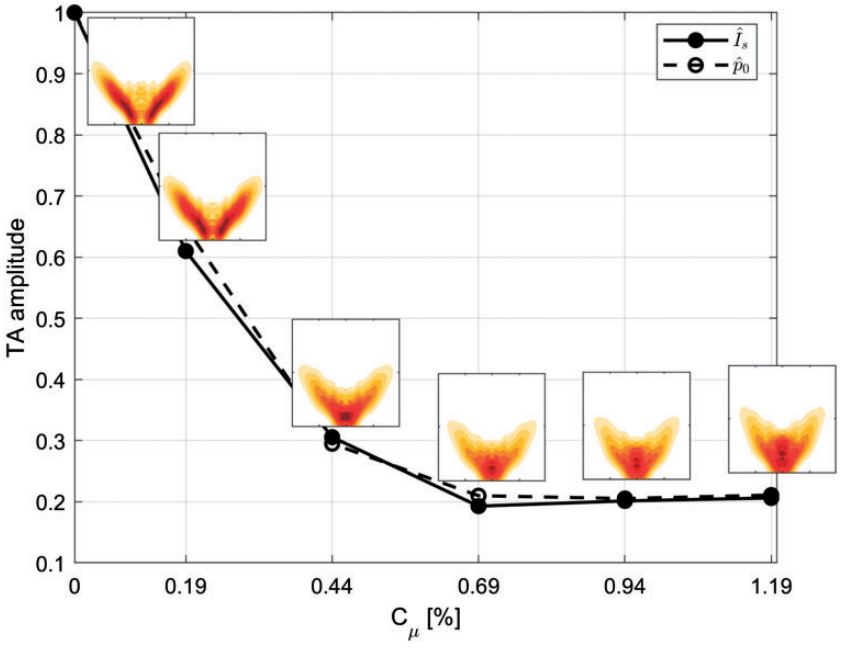

Figure 16. Amplitude of global symmetric OH*-fluctuations $\hat{I}_s$ (black solid) and decomposed pressure signals of mode $m = 0$ ($\hat{p}_0$, black dotted) for different actuation amplitudes in thermoacoustically unstable partially premixed flames at Re = 22,000, $\phi = 0.71$, and $f_{\mathrm{PVC}} = 118$ Hz; values are normalized with respect to the non-actuated case ($C_\mu = 0$).

conclude that the impact of the PVC actuation on the equivalence ratio fluctuations is crucial as well to understand the damping mechanism for the partially premixed flame.

To further investigate the damping of the thermoacoustic oscillations through the PVC actuation, a parameter study is conducted, where the actuation amplitude was stepwise increased. Figure 16 shows the amplitude of the thermoacoustic oscillation as derived from the symmetric pressure and OH*-spectra versus the PVC actuation amplitude. The corresponding mean flame shapes are also shown revealing the movement of the major heat release zone from the flame arms to the flame root, which ends up in a more compact flame. Strikingly, even for the lowest actuation amplitude of , a reduction of the thermoacoustic pulsations of 40% is achieved. Upon further increasing the actuation amplitude, the thermoacoustic oscillations are suppressed by 80% at $C_\mu \geq 0.69\%$, which is the most remarkable effect of the actuation. The pressure and OH*-fluctuation curve are almost identical for all actuation amplitudes, which underline the overall suppression of pressure and flame fluctuations induced by thermoacoustic oscillations.

5. Conclusion

This study investigates the impact of helical open-loop PVC excitation on thermoacoustically stable and unstable swirl-stabilized flames as well as the isothermal combustor flow. The considered reacting cases are thermoacoustically stable and unstable attached V-flames without a natural PVC and stable detached M-flames with naturally occurring PVC.

The present control scheme is motivated by the recent findings from linear stability theory that determine that the PVC is a self-excited global mode. The actuator was implemented into a centerbody upstream of the flame where theory predicts the highest receptivity of the PVC mode to open-loop control. In this manner, the actuation neatly locks to the natural instability of the flow and allows for a very effective control and minimal input energy.

The isothermal combustor flow was studied first regarding the impact of the PVC actuation on mode shape and flow dynamics. This was done using SPOD of time-resolved PIV snapshots. The corresponding lock-in study serves as a proof of concept for the active flow control principal.

For the reacting cases, time-resolved OH*-chemiluminescence measurements were conducted. The symmetric and antisymmetric global OH*-fluctuation signal was Fourier decomposed and analyzed in conjunction with pressure measurements which allows for characterization of interactions between the hydrodynamic modes and the flame. To reveal the impact of the PVC actuation on the flame shape, the deconvoluted mean and Fourier-decomposed OH* distributions were considered.

From this experimental study, the following conclusions can be drawn:

1. The current control unit allows for direct actuation of the PVC at extremely low actuation amplitudes (less than 1% of total momentum). This is possible because the actuation is applied at the most sensitive region of the PVC as determined from stability theory.
2. Lock-in experiments show that the actuation is acting directly on the PVC instability, without qualitatively altering the flow dynamics.
3. The control works equally effective for reacting and non-reacting conditions.
4. The PVC can be excited even in flames subjected to severe thermoacoustic oscillations.
5. At perfectly premixed conditions, the PVC actuation causes no relevant reduction of the amplitude of the thermoacoustic oscillations. However, nonlinear interactions are observable that manifest in non-symmetric heat release.
6. PVC actuation enhances turbulence at the flame root region, which causes more compact and more upstream located flames. This leads to a slight increase of the frequency of the thermoacoustic instability due to a reduction of convective time lags and change in the phase relation between heat and pressure fluctuations.[55–57]
7. For partially premixed flames, the PVC actuation causes a reduction of the thermoacoustic instability of 80% at an actuation amplitude of less than 1%. Current experiments suggest that the suppression is caused by the mitigation of equivalence ratio fluctuations due to the PVC-enhanced mixing.

The observations regarding PVC-induced flame dynamics reported here are in line with the current literature, which shows that this flow control system is capable to generate proper experimental conditions to study flame dynamics and mode interaction in a controlled manner. Moreover, the open-loop control of the M-flame configuration and the SPOD-based lock-in study of the isothermal flow shows that the actuator does not trigger any undesired modes other than the naturally occurring PVC. This is highly important for the results of the present and follow-up studies that focus on the exclusive influence of the PVC on the combustion processes. From an application point of view, this study shows that by exploiting the PVC instability, thermoacoustic oscillations can be effectively suppressed for some flames using very little input energy. In conjunction with other studies cited above, it

appears that the PVC can be employed as a beneficial tool in reacting flows, provided that it is controlled properly. In real gas turbines, where pressure and velocity are significantly higher as in a lab-scale burner, the share of the PVC on the total energy is expected not to change. As a consequence, very strong PVC-induced fluctuation could occur. Therefore, efficient PVC control in real gas turbines can play an important role to maintain stability of the system.

Acknowledgements

Special thanks go out to Andy Göhrs and Robert Bahnweg for their technical support and Alexander Jaeschke for supporting the experimental procedure.

Declaration of Conflicting Interests

The author(s) declared no potential conflicts of interest with respect to the research, authorship, and/or publication of this article.

Funding

The author(s) disclosed receipt of the following financial support for the research, authorship, and/or publication of this article: Deutsche Forschungsgemeinschaft (DFG) within the project OB 402/4-3. We acknowledge support by the German Research Foundation and the Open Access Publication Fund of TU Berlin.

ORCID iD

Finn Lückoff https://orcid.org/0000-0002-6610-0851

References

1. Gallaire F, Ruith M, Meiburg E, et al. Spiral vortex breakdown as a global mode. *J Fluid Mech* 2006; 549: 71–80.
2. Petz C, Hege HC, Oberleithner K, et al. Global modes in a swirling jet undergoing vortex breakdown. *Phys Fluids* 2011; 23(9): 091102.
3. Oberleithner K, Terhaar S, Rukes L, et al. Why nonuniform density suppresses the precessing vortex core? *J Eng Gas Turb Power* 2013; 135(12): 121506.
4. Terhaar S, Oberleithner K and Paschereit C. Key parameters governing the precessing vortex core in reacting flows: an experimental and analytical study. *Proc Combust Inst* 2015; 35(3): 3347–3354.
5. Oberleithner K, Stöhr M, Im SH, et al. Formation and flame-induced suppression of the precessing vortex core in a swirl combustor: experiments and linear stability analysis. *Combust Flame* 2015; 162(8): 3100–3114.
6. Syred N. A review of oscillation mechanisms and the role of the precessing vortex core (PVC) in swirl combustion systems. *Prog Energy Combust Sci* 2006; 32(2): 93–161.
7. Huang Y and Yang V. Dynamics and stability of lean-premixed swirl-stabilized combustion. *Prog Energy Combust Sci* 2009; 35(4): 293–364.
8. Candel S, Durox D, Schuller T, et al. Dynamics of swirling flames. *Annu Rev Fluid Mech* 2014; 46: 147–173.
9. Stöhr M, Boxx I, Carter CD, et al. Experimental study of vortex flame interaction in a gas turbine model combustor. *Combust Flame* 2012; 159: 2636–2649.
10. Stöhr M, Arndt C and Meier W. Effects of Damköhler number on vortex–flame interaction in a gas turbine model combustor. *Proc Combust Inst* 2013; 34(2): 3107–3115.
11. An Q, Kwong WY, Geraedts BD, et al. Coupled dynamics of lift-off and precessing vortex core formation in swirl flames. *Combust Flame* 2016; 168: 228–239.
12. Stöhr M, Oberleithner K, Sieber M, et al. Experimental study of transient mechanisms of bi-stable flame shape transitions in a swirl combustor. *J Eng Gas Turbines Power* 2018; 140: 011503.
13. Stöhr M, Oberleithner K, Arndt CM, et al. Experimental study of transient coupling of PVC formation and flame shape transition in a bi-stable turbulent swirl flame. In: *Proceedings of the 7th European combustion meeting, Budapest, Hungary, 2015*.
14. Steinberg A, Boxx I, Stoehr M, et al. Flow-flame interactions causing acoustically coupled heat release fluctuations in a thermo-acoustically unstable gas turbine model combustor. *Combust Flame* 2010; 157(12): 2250–2266.
15. Terhaar S, Krüger O and Paschereit CO. Flow field and flame dynamics of swirling methane and hydrogen flames at dry and steam-diluted conditions. *J Eng Gas Turbine Power* 2015; 137: 041503.
16. Stöhr M, Arndt C and Meier W. Transient effects of fuel-air mixing in a partially-premixed turbulent swirl flame. *Proc Combust Inst* 2015; 35(3): 3327–3335.
17. Galley D, Ducruix S, Lacas F, et al. Mixing and stabilization study of a partially premixed swirling flame using laser induced fluorescence. *Combust Flame* 2011; 158(1): 155–171.
18. Mathews B, Hansford S and O'Connor J. Impact of swirling flow structure on shear layer vorticity fluctuation mechanisms. In: *ASME turbo expo 2018: turbomachinery technical conference and exposition, volume 4A: combustion, fuels and emissions*, Oslo, Norway, 11–15 June 2018. New York: ASME.
19. Frederick M, Manoharan K, Dudash J, et al. Impact of PVC dynamics on shear layer response in a swirling jet. *J Eng Gas Turb Power* 2018; 140: 061503.
20. Oberleithner K, Paschereit CO and Wygnanski I. On the impact of swirl on the growth of coherent structures. *J Fluid Mech* 2014; 741: 156–199.
21. Terhaar S, Ćosić B, Paschereit C, et al. Suppression and excitation of the precessing vortex core by acoustic velocity fluctuations: an experimental and analytical study. *Combust Flame* 2016; 172: 234–251.
22. Ghani A, Poinsot T, Gicquel L, et al. LES study of transverse acoustic instabilities in a swirled kerosene/air combustion chamber. *Flow Turbul Combust* 2016; 96(1): 207–226.
23. Steinberg A, Arndt C and Meier W. Parametric study of vortex structures and their dynamics in swirl-stabilized combustion. *Proc Combust Inst* 2013; 34: 3117–3125.
24. Moeck JP, Bourgouin JF, Durox D, et al. Nonlinear interaction between a precessing vortex core and acoustic

oscillations in a turbulent swirling flame. *Combust Flame* 2012; 159(8): 2650–2668.
25. Palies P, Ilak M and Cheng R. Transient and limit cycle combustion dynamics analysis of turbulent premixed swirling flames. *J Fluid Mech* 2017; 830: 681–707.
26. Paredes P, Terhaar S, Oberleithner K, et al. Global and local hydrodynamic stability analysis as a tool for combustor dynamics modeling. In: *Proceedings of the ASME turbo expo* 2015; 138: 021504.
27. Oberleithner K, Sieber M, Nayeri CN, et al. Three-dimensional coherent structures in a swirling jet undergoing vortex breakdown: stability analysis and empirical mode construction. *J Fluid Mech* 2011; 679: 383–414.
28. Qadri UA, Mistry D and Juniper MP. Structural sensitivity of spiral vortex breakdown. *J Fluid Mech* 2013; 720: 558–581.
29. Tammisola O and Juniper M. Coherent structures in a swirl injector at Re=4800 by nonlinear simulations and linear global modes. *J Fluid Mech* 2016; 792: 620–657.
30. Kaiser TL, Poinsot T and Oberleithner K. Stability and sensitivity analysis of hydrodynamic instabilities in industrial swirled injection systems. *J Eng Gas Turb Power* 2018; 140(5): 051506.
31. Rukes L, Paschereit CO and Oberleithner K. An assessment of turbulence models for linear hydrodynamic stability analysis of strongly swirling jets. *Eur J Mech B Fluid* 2016; 59: 205–218.
32. Müller JS, Lückoff F and Oberleithner K. Guiding actuator designs for active flow control of the precessing vortex core by adjoint linear stability analysis. *J Eng Gas Turb Power* 2018; 144(4): 041028.
33. Hill DC. Adjoint systems and their role in the receptivity problem for boundary layers. *J Fluid Mech* 1995; 292: 183–204.
34. Magri L and Juniper M. Global modes, receptivity, and sensitivity analysis of diffusion flames coupled with duct acoustics. *J Fluid Mech* 2014; 752: 237–265.
35. Kuhn P, Moeck JP, Paschereit CO, et al. Control of the precessing vortex core by open and closed-loop forcing in the jet core. In: *ASME turbo expo 2016: turbomachinery technical conference and exposition, volume 4B: combustion, fuels and emissions*, Seoul, South Korea, 13–17 June 2016. p.13.
36. Lückoff F, Sieber M, Paschereit CO, et al. Characterization of different actuator designs for the control of the precessing vortex core in a swirl-stabilized combustor. *J Eng Gas Turb Power* 2017; 140(4): 041503–041503-10.
37. Lückoff F, Sieber M and Oberleithner K. Open-loop control of the precessing vortex core in a swirl-stabilized combustor: impact on flame shape and flame stability. In: *Proceedings of ASME turbo expo 2018: turbomachinery technical conference and exposition*, Lillestrøm, Norway, 11–15 June 2018. GT2018-75472.
38. Sieber M, Ostermann F, Woszidlo R, et al. Lagrangian coherent structures in the flow field of a fluidic oscillator. *Phys Rev Fluid* 2016; 1(5): 050509.
39. Schimek S, Moeck JP and Paschereit CO. An experimental investigation of the nonlinear response of an atmospheric swirl-stabilized premixed flame. *J Eng Gas Turb Power* 2011; 133(10): 101502.
40. Leuckel W. *Swirl intensities, swirl types and energy losses of different swirl generating devices*. Technical report, Doc. No. G02/a/16, International Flame Research Foundation, Ijmuiden, The Netherlands, 1967.
41. Greenblatt D and Wygnanski IJ. The control of flow separation by periodic excitation. *Prog Aerosp Sci* 2000; 36(7): 487–545.
42. Soria J. An investigation of the near wake of a circular cylinder using a video-based digital cross-correlation particle image velocimetry technique. *Exp Therm Fluid Sci* 1996; 12: 221–233.
43. Huang HT, Fiedler HE and Wang JJ. Limitation and improvement of PIV. *Exp Fluid* 1993; 15(4–5): 263–273.
44. Sieber M, Paschereit CO and Oberleithner K. Spectral proper orthogonal decomposition. *J Fluid Mech* 2016; 792: 798–828.
45. Holmes P, Lumley JL and Berkooz G. *Turbulence, coherent structures, dynamical systems and symmetry*. Cambridge: Cambridge University Press, 1998.
46. Sieber M, Paschereit CO and Oberleithner K. Advanced identification of coherent structures in swirl-stabilized combustors. *J Eng Gas Turb Power* 2016; 139: 021503–021503-8.
47. Acharya VS, Shin DH and Lieuwen T. Premixed flames excited by helical disturbances: flame wrinkling and heat release oscillations. *J Propul Power* 2013; 29(6): 1282–1291.
48. Moeck JP, Bourgouin JF, Durox D, et al. Tomographic reconstruction of heat release rate perturbations induced by helical modes in turbulent swirl flames. *Exp Fluid* 2013; 54(4): 1–17.
49. Li LKB and Juniper MP. Lock-in and quasiperiodicity in a forced hydrodynamically self-excited jet. *J Fluid Mech* 2013; 726: 624–655.
50. Oberleithner K, Rukes L and Soria J. Mean flow stability analysis of oscillating jet experiments. *J Fluid Mech* 2014; 757: 1–32.
51. Li LK and Juniper M. Phase trapping and slipping in a forced hydrodynamically self-excited jet. *J Fluid Mech*. Epub ahead of print 29 October 2013. DOI: 10.1017/jfm.2013.533.
52. Oberleithner K, Schimek S and Paschereit CO. Shear flow instabilities in swirl-stabilized combustors and their impact on the amplitude dependent flame response: a linear stability analysis. *Combust Flame* 2014; 162(1): 86–99.
53. Frederick M, Manoharan K, Dudash J, et al. Impact of precessing vortex core dynamics on shear layer response in a swirling jet. *J Eng Gas Turb Power* 2018; 140(6): 061503.
54. Oberleithner K and Paschereit CO. Modeling flame describing functions based on hydrodynamic linear stability analysis. In: *ASME turbo expo 2016: turbomachinery technical conference and exposition, vol. 4B: combustion, fuels and emissions*, Seoul, South Korea, 13–17 June 2016. New York: ASME.
55. Silva CF and Polifke W. Non-dimensional groups for similarity analysis of thermoacoustic instabilities. *Proc Combust Inst* 2019; 37(4): 5289–5297.
56. Rayleigh. The explanation of certain acoustical phenomena. *Nature* 1878; 18(455): 319–321.

57. Juniper MP and Sujith RI. Sensitivity and nonlinearity in thermoacoustics. *Annu Rev Fluid Mech* 2018; 50: 661–689.
58. Lieuwen T and Zinn BT. Theoretical investigation of combustion instability mechanisms in lean premixed gas turbines. AIAA Paper 98-0641.
59. Lieuwen T, Torres H, Johnson C, et al. A mechanism of combustion instability in lean premixed gas turbine combustors. *J Eng Gas Turb Power* 2001; 123(1): 182–189.
60. Ćosić B, Terhaar S, Moeck JP, et al. Response of a swirl-stabilized flame to simultaneous perturbations in equivalence ratio and velocity at high oscillation amplitudes. *Combust Flame* 2014; 162(4): 1046–1062.